

The ALMaQUEST Survey X: What powers merger induced star formation?

Mallory D. Thorp^{1*}, Sara L. Ellison¹, Hsi-An Pan², Lihwai Lin³, David R. Patton⁴, Asa F. L. Bluck^{5,6}, Dan Walters¹, Jillian M. Scudder⁷

¹*Department of Physics & Astronomy, University of Victoria, Finnerty Road, Victoria, British Columbia, V8P 1A1, Canada*

²*Department of Physics, Tamkang University, Tamsui Dist., New Taipei City 251301, Taiwan*

³*Institute of Astronomy & Astrophysics, Academia Sinica, Taipei 10617, Taiwan*

⁴*Department of Physics & Astronomy, Trent University, 1600 West Bank Drive, Peterborough, ON K9L 0G2, Canada*

⁵*Department of Physics, Florida International University, 11200 SW St., Miami, FL, USA*

⁶*Hughes Hall College, University of Cambridge, Wollaston Road, Cambridge CB1 2EW, UK*

⁷*Department of Physics & Astronomy, Oberlin College, Oberlin, OH, 44074, USA*

Accepted XXX. Received YYY; in original form ZZZ

ABSTRACT

Galaxy mergers are known to trigger both extended and central star formation. However, what remains to be understood is whether this triggered star formation is facilitated by enhanced star formation efficiencies, or an abundance of molecular gas fuel. This work presents spatially resolved measurements of CO emission collected with the Atacama Large Millimetre Array (ALMA) for 20 merging galaxies (either pairs or post-mergers) selected from the Mapping Nearby Galaxies at Apache Point Observatory (MaNGA) survey. Eleven additional merging galaxies are selected from the ALMA MaNGA QUenching and STar formation (ALMaQUEST) survey, resulting in a set of 31 mergers at various stages of interaction and covering a broad range of star formation rates (SFR). We investigate galaxy-to-galaxy variations in the resolved Kennicutt-Schmidt relation, (rKS: Σ_{H_2} vs. Σ_{SFR}), the resolved molecular gas main sequence (rMGMS: Σ_{\star} vs. Σ_{H_2}), and the resolved star-forming main sequence (rSFMS: Σ_{\star} vs. Σ_{SFR}). We quantify offsets from these resolved relations to determine if star formation rate, molecular gas fraction, and/or star formation efficiency (SFE) is enhanced in different regions of an individual galaxy. By comparing offsets in all three parameters we can discern whether gas fraction or SFE powers an enhanced Σ_{SFR} . We find that merger-induced star formation can be driven by a variety of mechanisms, both within a galaxy and between different mergers, regardless of interaction stage.

Key words: galaxies: interactions – galaxies: star formation – galaxies: evolution

1 INTRODUCTION

Evidence has consistently demonstrated that galaxy-galaxy mergers can trigger star formation: from the bluer colour of peculiar galaxies (Larson & Tinsley 1978; Barton Gillespie et al. 2003; Lambas et al. 2012) and excess H α emission noted in interacting pairs (Kennicutt et al. 1987; Knapen & James 2009), to large single-fibre spectroscopic surveys revealing an excess of star formation as a merger event progresses (Ellison et al. 2008; Woods et al. 2010; Scudder et al. 2012; Patton et al. 2013; Knapen et al. 2015). Hydrodynamical simulations illustrate how induced star formation likely stems from gas losing angular momentum and fueling centralized star formation, as a result of the non-axisymmetric structures generated by gravitational forces in an interaction (Barnes & Hernquist 1991; Mihos & Hernquist 1996; Iono et al. 2004; Hopkins et al. 2013). The degree to which star formation is enhanced can vary drastically depending on the properties of an interaction, with orbital parameters (Di Matteo et al. 2007; D’Onghia et al. 2010; Moreno et al. 2015), mass ratio between constituents (Cox et al. 2006, 2008) and gas fraction of the

interacting disk (Bournaud et al. 2011; Perez et al. 2011; Scudder et al. 2015; Fensch et al. 2017) all leading to varied star formation strengths. In simulations, star formation tends to peak when the interacting galaxies are either close to pericentric passage or at the moment of coalescence (Lotz et al. 2008; Scudder et al. 2012; Hani et al. 2020). Such results are supported by observational evidence, which has consistently demonstrated that global star formation rate values are greatest for interactions with equal mass ratios and small projected separations (Nikolic et al. 2004; Lin et al. 2007; Ellison et al. 2008; Woods et al. 2010; Scudder et al. 2012; Ellison et al. 2013; Bickley et al. 2022).

Resolved spectroscopic studies have revealed further complexity of merger-induced star formation on a local scale. Integral Field Spectroscopy (IFS) surveys such as the MaNGA Survey (Bundy et al. 2015), the Calar Alto Legacy Integral Field Area Survey (CALIFA, Sánchez et al. 2012), and the Sydney-Australian Astronomical Observatory Multi-object Integral field spectrograph Survey (SAMI, Allen et al. 2015) have allowed for the collection of resolved spectroscopic data of large samples of galaxies from which robust statistical results can be attained. Investigations of interacting galaxy pairs in IFS surveys have further corroborated the central enhancement of

* E-mail: mallorythorp@uvic.ca

star formation noted in global studies, but often find a diversity of behaviours in the outskirts of the galaxy where star formation can be unaffected, enhanced, or suppressed (Barrera-Ballesteros et al. 2015; Pan et al. 2019; Steffen et al. 2021). Such variation may be linked to the global galaxy properties, with only the higher mass galaxy in a pair showing enhanced star formation in the outskirts (Steffen et al. 2021). However, evidence also suggests only galaxies at pericentre and coalescence have elevated star formation at large radii (Pan et al. 2019). Significant variations in spatial star formation enhancement are therefore apparent even in a single stage of interaction.

Whereas pairs of galaxies represent the pre-merger regime, post-merger galaxies allow us to study the late stages of the interaction sequence. On average, post-mergers have central star formation enhancements that moderately fall off with radius, but galaxies with similar central star formation enhancements can have enhanced, normal, or suppressed star formation in the outskirts (Thorp et al. 2019). Just as the unique properties of a galaxy and its interaction parameters can lead to a diverse range of global star formation enhancement, there is equal if not greater complexity when star formation is examined on the resolved scale.

A stepping stone towards understanding the variation of star formation seen in merging galaxies is to characterize the gas which fuels star formation on a kpc-scale. The tight correlation between star formation rate (SFR) and molecular gas mass (M_{H_2}) which exists on a global scale (often called the Kennicutt-Schmidt relation for its flagship publications Schmidt 1959 and Kennicutt 1989) exists on a local scale as well, resulting in the resolved Kennicutt-Schmidt (rKS) (Bigiel et al. 2008; Leroy et al. 2008; Schruba et al. 2011). A high star formation efficiency ($SFE = SFR/M_{H_2}$) can lead to regions notably above the rKS from a local boost in star formation (Leroy et al. 2013; Bolatto et al. 2017; Utomo et al. 2017). Offsets from the rKS are the primary driver of offsets in the resolved star-forming main sequence (rSFMS, the strong correlation between Σ_{SFR} and Σ_\star ; Sánchez et al. 2013; Cano-Díaz et al. 2016; González Delgado et al. 2016), demonstrating that although the star formation rate surface density (Σ_{SFR}) is regulated by molecular gas mass surface density (Σ_{H_2}) as predicted by the rKS, more varied behaviour in star formation stems from changes in SFE (Ellison et al. 2020b).

However, there are other ways star formation can be augmented, such as a high gas surface density to fuel stellar growth (Bigiel et al. 2008; Leroy et al. 2013; Schruba et al. 2011). A surplus of molecular gas manifests as an offset from the correlation between Σ_{H_2} and the stellar mass surface density (Σ_\star), otherwise known as the resolved molecular gas main sequence (rMGMS, Wong et al. 2013; Lin et al. 2019; Ellison et al. 2021a). Environmental effects on the Σ_\star profile can also boost star formation (Usero et al. 2015; Gallagher et al. 2018; Jiménez-Donaire et al. 2019). Examining how mergers deviate from the rKS and rMGMS will help discern what drives enhancements in star formation on a kpc-scale.

Several attempts have been made to pinpoint the relative importance of the total molecular gas fraction ($f_{H_2} = M_{H_2}/M_\star$) and the SFE to driving enhanced star formation in mergers. Early studies measuring total molecular gas mass with single dish telescopes found conflicting results concerning whether total molecular gas fraction or star formation efficiency drives enhanced star formation in mergers (Braine & Combes 1992; Casasola et al. 2004; Huchtmeier et al. 2008). More recent studies have leaned towards an enhanced gas fraction driving star formation in both interacting pair (Violino et al. 2018; Pan et al. 2018) and post-merger galaxies (Ellison et al. 2018). SFEs for merging galaxies are mostly normal, except for very close pairs and equal-mass systems whose violent interactions lead to en-

hanced SFEs (Pan et al. 2018). What remains unclear is how these global properties drive kpc-scale variations in star formation.

Only recently have observations of resolved molecular gas properties been collected for large samples to complement large optical IFS surveys, allowing for the combined analysis of Σ_{H_2} and Σ_{SFR} . The Extragalactic Database for Galaxy Evolution (EDGE) - CALIFA survey (Bolatto et al. 2017) targeted 126 CALIFA galaxies with the Combined Array for Millimeter-wave Astronomy (CARMA) to investigate depletion time gradients within galaxies (Utomo et al. 2017; Colombo et al. 2018) and the processes which regulate star formation on a kpc-scale (Barrera-Ballesteros et al. 2021). The ALMA-MaNGA QUenching and STar formation (ALMaQUEST) survey (Lin et al. 2020) observed MaNGA galaxies with ALMA to not only confirm that the key scaling relations between star formation rate, molecular gas, and stellar mass that exist on a global scale stem from a kpc-scale relationship, but also that the resolved star-forming main sequence is likely the result of the two other relations (Lin et al. 2019; Ellison et al. 2021a; Baker et al. 2022). ALMaQUEST has also revealed that even though the absolute star formation rate in a galaxy is primarily driven by the amount of molecular gas, the scatter in the resolved star formation efficiency is mostly driven by local changes in SFE (Ellison et al. 2020a). Given that variations in star formation in the outskirts of mergers are by definition scatter from the rSFMS, such a result might imply that SFE may drive star formation for individual regions of galaxy, even if globally gas reservoir is the dominant driver. Further investigation of the interplay between star formation and molecular gas has been done on the scale of molecular clouds with the Physics at High Angular resolution in Nearby Galaxies (PHANGS)-ALMA survey (Leroy et al. 2021). With resolution on the order of ~ 100 pc, PHANGS-ALMA found greater scatter in all three scaling relations compared to lower-resolution studies, revealing significant variation in star formation and molecular gas content even within similar morphological environments (Pessa et al. 2021; Querejeta et al. 2021).

Although EDGE-CALIFA, the largest of surveys of this kind, does have a small number of mergers that may be responsible for changes in SFR and depletion times (Bolatto et al. 2017; Utomo et al. 2017; Chown et al. 2019), none of the surveys with both IFS and molecular gas data have a sufficient number of mergers to make a dedicated study of interaction induced physics. A handful of detailed case-studies of the resolved star-formation efficiency of pre-merger galaxies have been completed, revealing significant diversity of depletion time on a resolved scale (Tomičić et al. 2018; Bemis & Wilson 2019). A study dedicated to a diverse sample of merging and post-merger galaxies is required to better understand the most extreme variations in star formation and gas properties.

In the present work we have observed a sample of 31 merging galaxies with a broad range of interaction progressions and star formation rates, with the specific goal of investigating how merger properties effect the mechanisms which drive star formation. Eleven of these mergers are taken from the main ALMaQUEST sample (Lin et al. 2020), plus we present observations for 20 additional galaxies with new CO(1-0) data obtained from ALMA. Together, we refer to this sample of 31 galaxies as the ALMaQUEST merger sample. In this paper, we aim to distinguish whether star formation efficiency or molecular gas fraction drives spatial changes in star formation rate. In Pan et al. (in prep) we will further investigate how the resolved star formation and gas properties vary with merger configuration.

In Section 2 we describe our methods for selecting a sample of mergers, as well as the MaNGA and ALMA observations utilized in this investigation. Section 3 presents our main results, comparing individual resolved scaling relations for our merger sample, as well

as comparing offsets from all three scaling relations. We summarize the impact of this work in Section 4. Throughout the work we adopt a cosmology in which $H_0 = 70$ km/s/Mpc, $\Omega_M = 0.3$, and $\Omega_\Lambda = 0.7$.

2 DATA

2.1 Merger Sample Selection

Our sample of merging galaxies is collected from the MaNGA data release 15 (DR15), which was the most recent publicly available release at the time of our observations and for the duration of this project. We visually classify post-merger and interacting galaxies from the ~ 4800 galaxies in DR15 using the Sloan Digital Sky Survey (SDSS) Sky Server *gri*-images (*r*-band half-light surface brightness limit of 23.0 mag arcsec⁻²; Strauss et al. 2002). Post-merger galaxies are distinguished by clear morphological disturbances indicating a recent interaction, such as tidal tails or shells, but with no obvious companion. Galaxies in an interacting pair are identified with similar indicators, with the addition of a clear visual connection to a second disturbed galaxy (such as tidal bridges).

Beyond the visually selected sample, we also identify a group of spectroscopic pairs, where a visible connection between a galaxy and a possible companion is unclear, but spatial and redshift information reveal the two galaxies may be interacting. Spectroscopic pairs are selected using the Patton et al. (2016) catalogue, which provides the closest companion for each galaxy in SDSS data release 7 (DR7), with a companion boundary at projected separation $r_p = 1$ Mpc and a maximum difference in velocity between the two of $\Delta v = 1000$ km/s. We assume any MaNGA galaxies with a projected separation less than 2'' from the Patton et al. (2016) galaxy position are the same object. We limit our spectroscopic pairs to those with a mass ratio between 0.1 and 10 (meaning the smaller of the pair is more than 10% the mass of the larger), and only include galaxies whose companion is within $r_p < 100$ kpc and $\Delta v < 500$ km/s. For simplicity, the rest of this work will not distinguish visually and spectroscopically selected pairs; we will simply refer to “pairs”. The combination of the pair and post-merger galaxies yields a total sample of 903 galaxies in DR15 which we hence refer to as the parent merger sample, from which we can select a subsample for ALMA observations.

To select candidate mergers for ALMA observations we first exclude all mergers with declination greater than 20°, leaving only those with positions that overlap with ALMA’s observational range. From the initial parent merger sample only 143 galaxies meet this criterion. We next select mergers for which our target CO line S/N can be achieved in less than 5 hours, to ensure we can observe as many mergers as possible within a competitive proposal (see Section 2.2 for more details). What remains is a sample of 6 post-mergers and 14 pairs, which are observed as part of an ALMA Cycle 7 program (2019.1.00260.S, P.I.: Hsi-An Pan, details in Section 2.2). We also make use of eleven galaxies from the ALMaQUEST survey that show clear signs of an interaction within our classification scheme: 8 post-mergers and 3 pairs (Lin et al. 2020; Ellison et al. 2020a). The SDSS *gri*-images of three of the galaxies in the final ALMaQUEST merger sample are included in the left panels of Figure 1 (continued for all mergers in Appendix A). The final sample of 14 post-merger and 17 pair galaxies is summarized in Table 1. Included in the table are key global properties from the MaNGA PIPE3D Value Added Catalogue (VAC) including total stellar mass (M_\star), total star formation rate (SFR), and redshift (z). We also include the offset from the global star-forming main sequence ΔSFR , where $\Delta\text{SFR} = \log \text{SFR}_{\text{galaxy}} - \log \text{SFR}_{\text{control}}$. $\text{SFR}_{\text{control}}$ is the median SFR value of galaxies within 2σ of a fit to the star-forming

main sequence (controls are also matched within 0.1 dex in M_\star and 0.005 in z). Merger properties are listed as well, including r_p , Δv , and mass ratio. Post-merger galaxies have empty r_p , Δv , and mass ratio values since there is no companion with which to compare. Pair galaxies that were visually identified do not have measured Δv and mass ratio values, since there is no spectroscopic information from their companion.

The merger sample covers a broad range of M_\star and SFR. Figure 2 compares these properties for our post-merger (orange circles) and pair (triangles) galaxies with respect to the rest of MaNGA, shown as grey hexbins. Pairs are colour-coded by the projected separation from their closest companion. Our sample is representative of a typical merger sample, containing galaxies with both greatly elevated and comparatively low SFRs. The inset histogram of Figure 2 shows the distribution of the offset from the star-forming main sequence ΔSFR of our post-merger (orange) and pair (blue) galaxies with respect to the rest of MaNGA (grey). Although the pair and post-merger samples have on average larger ΔSFR values than non-interacting galaxies, we still cover a broad range of ΔSFR values to reflect the overall variety of behaviours seen in larger galaxy merger studies and to probe any corresponding diversity in the molecular gas properties of those mergers. We note that there may be some selection bias in the sample, given some post-mergers come from the ALMaQUEST starburst sample of Ellison et al. (2020a), and the rest still need to have enough gas for detectable CO as described in the following section.

2.2 ALMA Observations

Observations of CO $J = 1 \rightarrow 0$ (CO hereafter), rest frame 115 GHz, were completed for 6 post-merger and 14 pair galaxies as part of Cycle 7 ALMA program 2019.1.00260.S (P.I.: Hsi-An Pan). The remaining 11 mergers were already available from the original ALMaQUEST sample (Lin et al. 2020). Cycle 7 observations were designed to replicate the methodology used in the original ALMaQUEST survey, the details of which can be found in the survey paper by Lin et al. (2020). We provide a brief summary of those techniques below.

Observations were carried out using the Band 3 receiver, taken in the C43-2 configuration to achieve a synthesized beam full-width half maximum (FWHM) of 2.5'' in order to match the effective resolution of the MaNGA survey (Law et al. 2015). The ALMA field of view in our chosen configuration is $\sim 50''$ which is sufficient to cover the MaNGA footprint for all of our galaxies. The spectral set up includes one high resolution spectral window targeting the CO emission (~ 10 km/s), and three low-resolution spectral windows around the target line to detect the continuum (~ 90 km/s). To reach a CO S/N greater than 3 for 50% of spaxels with $H\alpha$ S/N > 3, the on-target integration time varied between 0.1–3.3 hours. The same methodology is used for the main ALMaQUEST sample, ensuring consistent data quality between ALMaQUEST data and that acquired in Cycle 7 (Lin et al. 2017, 2020).

Data were calibrated using the ALMA data reduction software Common Astronomy Software Applications (CASA, McMullin et al. 2007) using version 5.4 for all but 3 galaxies (which were observed in earlier cycles and thus used CASA version 4.5), along with the standard ALMA reduction pipeline. In ALMA’s Band 3 the systematic flux uncertainty inherent with calibration is roughly 5–10% (Diaz Trigo et al. 2019). Continua were subtracted in the visibility domain for a handful of galaxies both in the original ALMaQUEST and the Cycle 7 galaxies. Once the continuum was subtracted, the task CLEAN was used to clean data down to 1σ and produce spectral line data cubes with a Briggs weighting (robust parameter=0.5), resulting

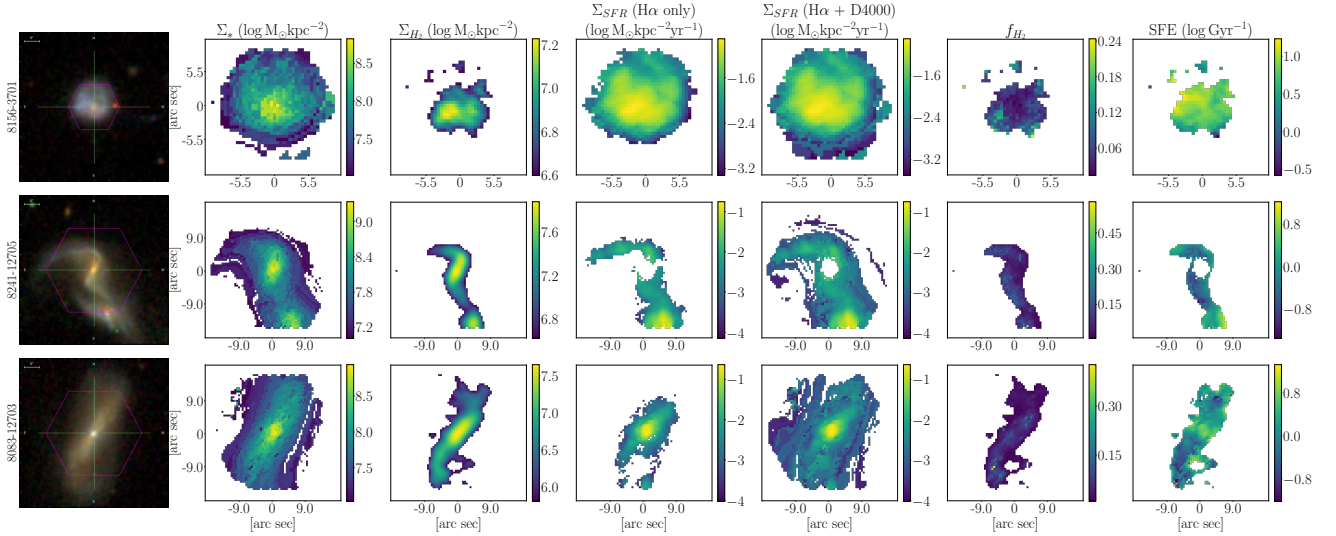


Figure 1. Data product maps for three of the galaxies in the ALMaQUEST merger sample (maps for the remaining 28 galaxies are available in Appendix A), a post-merger (top), a visual pair (middle), and a spectroscopic pair with the companion out of frame (bottom). From left to right: the SDSS *gri*-image, inclination corrected stellar mass surface density (from PIPE3D), inclination corrected molecular gas surface density (computed from CO luminosity), inclination corrected star formation rate surface density (computed from $H\alpha$ luminosity), inclination corrected star formation rate surface density (computed from $H\alpha$ luminosity and sSFR-D4000 relation), molecular gas fraction (Σ_{H_2}/Σ_*), and star formation efficiency ($\Sigma_{SFR}/\Sigma_{H_2}$). Note the significant increase in spaxel count when both $H\alpha$ and D4000 Σ_{SFR} are used. The central gap still present in the combined Σ_{SFR} map for 8241-12705 (second row, fifth column) is the result of D4000 exceeding 1.4 in those pixels. By including D4000- Σ_{SFR} measurements we optimize the overlap between Σ_{H_2} and Σ_{SFR} for our analysis.

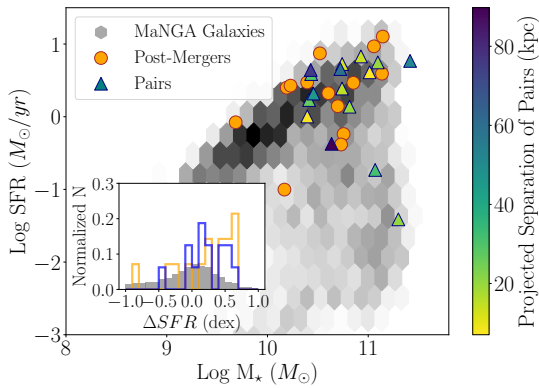


Figure 2. Position of our post-merger (orange circles) and pair (triangles) galaxies on the global star-forming main sequence defined by the rest of the MaNGA survey (grey hexbin). Pair galaxies are colour-coded by the projected separation from their closest companion (in kpc). Galaxies that were excluded due to a lack of viable CO spaxels are excluded from this diagram (see Table 1 and Subsection 2.2 for details). An inset histogram shows the distribution in ΔSFR for post-mergers (orange) and pair (blue) galaxies with respect to MaNGA (grey). Although our mergers probe more highly star-forming galaxies than a random population, our sample still covers a broad range of ΔSFR values.

in a native effective beam size ranging from $1.6''$ – $2.8''$ depending on the target. The data were then re-imaged with a user-specified spaxel size ($0.5''$) and a restoring beamsize ($2.5'' \times 2.5''$) to match the MaNGA image grid (prior) and spatial resolution (latter). The final cubes have channel widths of 11 km/s and $\sigma_{rms} \sim 0.2$ – 2 mJy/beam. We applied the CASA task IMMOMENTS to these datacubes to determine moment 0 (integrated intensity) maps. IMMOMENTS can

also generate moment 1 (intensity-weighted velocity) and moment 2 (intensity-weighted velocity dispersion) maps, but those are not relevant to the analysis of this work and are saved for future projects. Moment 0 maps are constructed by integrating the CO emission from a set velocity range without any clipping in signal. Table 1 lists the number of spaxels in each galaxy where the CO line emission from the moment 0 map has $S/N > 3$. Four of the merger galaxies observed as part of Cycle 7 (8615-1901, 8153-12702, 7968-12705, 8085-6101, all four early-type galaxies) have less than ten spaxels with $CO\ S/N > 3$, and are thus excluded from any further analysis that looks at individual galaxies (rather than spaxels).

The CO luminosity per spaxel determined from the moment 0 map is converted to molecular gas surface density Σ_{H_2} (M_\odot/kpc^2) using a constant conversion factor of $\alpha_{CO} = 4.35$ ($M_\odot (K\ km/s\ pc^2)^{-1}$) (Bolatto et al. 2013). All Σ_{H_2} values are then inclination corrected using the b/a axial ratios from the NASA Sloan Atlas (NSA) catalogue, themselves determined from single Sérsic fits. Three example Σ_{H_2} maps are provided in Figure 1, with the rest of the Σ_{H_2} maps from the sample available in Appendix A. There has been extensive research into the viability of a constant conversion factor, and many suggest using a metallicity dependent (Accurso et al. 2017; Sun et al. 2020) or metallicity and line intensity dependent (Narayanan et al. 2012) conversion instead. The requirements needed to determine accurate metallicity measurements would limit our spaxel count significantly, given the sparse overlap between high S/N star-forming spaxels and CO measurements (see Table 1), as we will discuss further in Subsection 2.3.1. To minimize the loss of spaxels we choose to use a constant conversion factor. In Appendix B we characterize the difference in Σ_{H_2} measurements when a metallicity dependent α_{CO} is used (for spaxels where that is possible), and confirm that key results from this work cannot result from inaccuracies of conversion factor.

Table 1. Summary of global properties of post-merger and pair galaxies observed with ALMA, with post-mergers first (no r_p values), followed by pairs ordered by r_p . Key global properties derived from the MaNGA VAC are included (M_\star , SFR, Δ SFR, z), as well as merger properties such as r_p , Δv , and mass ratio (the mass of the galaxy divided by that of its companion). Post-mergers have empty columns for merger properties, which require information about a companion galaxy. Pair galaxies that were visually identified only have r_p values, since spectroscopic information is not available for the companion. Also included are spaxel counts for each galaxy that meet our various star-forming and CO S/N cuts, along with the overlap between these regions. Galaxies with less than 10 spaxels of CO+SF($H\alpha$ +D4000) overlap are excluded for plots of individual galaxies.

plate-ifu	log M_\star	log SFR	Δ SFR	z	r_p	Δv	Mass Ratio	SF ($H\alpha$) # Spaxels	SF ($H\alpha$ +D4000) # Spaxels	CO S/N>3 # Spaxels	CO+SF ($H\alpha$) # Overlap	CO+SF ($H\alpha$ +D4000) # Overlap
	log M_\odot	log M_\odot/yr	dex		kpc	km/s						
9195-3702	11.14	1.10	0.62	0.064	-	-	-	0	53	204	0	5
9194-3702	11.06	0.97	0.52	0.075	-	-	-	0	811	379	0	328
8083-9101	11.14	0.59	0.11	0.038	-	-	-	331	1163	322	60	186
8952-12701	10.73	-0.38	-0.23	0.029	-	-	-	21	37	354	18	28
8084-3702	10.23	0.43	0.60	0.022	-	-	-	240	1007	552	150	531
8156-3701	10.52	0.87	0.66	0.053	-	-	-	778	941	279	279	279
8081-9101	10.60	0.32	0.23	0.028	-	-	-	321	600	436	255	335
8615-3703	10.19	0.40	0.45	0.018	-	-	-	324	997	538	276	519
9512-3704	10.70	0.14	-0.03	0.055	-	-	-	168	552	136	33	40
7977-12705	10.85	0.47	0.26	0.027	-	-	-	981	1472	538	197	201
8623-1902	10.17	-1.00	-0.84	0.025	-	-	-	4	175	257	2	87
8616-12702	10.76	-0.24	-0.40	0.031	-	-	-	469	1113	258	78	104
9195-3703	10.39	0.47	0.42	0.027	-	-	-	225	833	504	110	460
8615-1901	9.68	-0.08	0.51	0.020	-	-	-	461	588	2	2	2
8153-12702	9.90	-0.74	-0.45	0.038	0.46	-	-	333	1119	0	0	0
7975-6104	11.01	0.61	0.17	0.079	7.04	-	-	209	588	391	209	320
8241-12705	10.40	0.00	-0.05	0.027	8.23	80.0	3.14	847	1678	592	381	508
8082-9102	10.74	0.73	0.53	0.037	12.24	-	-	554	1197	668	422	591
7977-9102	10.93	0.83	0.41	0.063	13.78	-	-	524	1129	380	287	354
9195-9101	10.74	0.39	0.16	0.057	15.36	-	-	678	1797	722	455	675
8616-9101	11.10	0.75	0.28	0.092	19.89	276.0	4.19	112	1044	363	84	249
8078-12703	10.81	0.14	-0.02	0.028	20.20	102.0	-	1208	2597	1128	444	796
7968-12705	11.30	-1.41	-1.37	0.086	20.45	13.0	0.80	0	93	8	0	0
8078-6104	10.41	0.23	0.16	0.044	26.15	109.0	0.42	197	1039	433	153	431
8085-12701	10.43	0.59	0.61	0.030	29.51	-	-	2293	2601	458	456	458
8085-6101	11.07	-0.73	-1.09	0.052	31.48	-	-	0	0	2	0	0
8083-12703	10.46	0.32	0.24	0.025	45.24	60.6	-	822	2201	1264	641	1171
8082-12704	11.42	0.77	0.05	0.132	51.28	-	-	3	1617	451	3	244
8085-3704	10.72	0.66	0.43	0.037	58.73	37.0	0.89	319	727	608	299	552
8450-6102	10.43	0.64	0.54	0.042	75.35	102.0	1.81	1162	1550	536	503	536
8728-3701	10.64	-0.37	-0.49	0.028	89.75	113.0	1.96	0	31	156	0	0

2.3 MaNGA Data Products

The work presented here primarily uses MaNGA data products from the PIPE3D spectral fitting pipeline, described in detail in [Sánchez et al. \(2016a,b\)](#). Along with global values provided by the PIPE3D VAC mentioned previously, we also make extensive use of the PIPE3D stellar mass surface density (Σ_\star) and emission line fluxes. We correct all emission line fluxes for dust using a Milky Way dust extinction curve ([Cardelli et al. 1989](#)), assuming an intrinsic $H\alpha/H\beta$ ratio of 2.85. Star formation rate surface densities (Σ_{SFR}) are determined from the dust corrected $H\alpha$ luminosity using the [Kennicutt et al. \(1994\)](#) relation and assuming a Salpeter initial mass function ([Salpeter 1955](#)). Both Σ_\star and Σ_{SFR} are inclination corrected using the b/a axial ratios (derived from single Sérsic fits) provided in the NSA catalogue. The same b/a ratio is used to compute an inclination corrected galactocentric radius from the V-band centre of the MaNGA map. We also use the 4000Å break strength (D4000) provided by PIPE3D, as it serves a crucial role in expanding our star formation rate measurements described in the next section.

2.3.1 Star Formation Rates - D4000 vs $H\alpha$

The work presented here requires that both SFRs and molecular gas surface densities are measured in a given spaxel. Ideally we would use SFRs determined from $H\alpha$ and only consider the Σ_{SFR} values of star-forming spaxels defined by the [Kauffmann et al. \(2003\)](#) designation on a Baldwin, Phillips & Terlevich diagram (BPT; [Baldwin et al. 1981](#)). Along with a [Kauffmann et al. \(2003\)](#) star-forming cut, we also impose a S/N > 3 cut for the flux of each diagnostic emission line, as well as requiring an $H\alpha$ equivalent width (EW) > 6Å limit to ensure $H\alpha$ flux stems from a young stellar population. Of the 13,046 spaxels with CO detections S/N > 3, only 44.5% pass all of these star-forming criteria. Table 1 provides for each galaxy the total count of spaxels which pass the star-forming criteria cut for $H\alpha$, which have CO S/N > 3, and which pass both criteria.

To maximize the number of spaxels with both CO and SFR measurements, we elect to approximate Σ_{SFR} for spaxels that are not star-forming (based on our BPT and EW criteria) using the relationship between sSFR and D4000 found for both global ([Brinchmann et al. 2004](#)) and local ([Spindler et al. 2018](#); [Wang et al. 2019](#); [Bluck et al. 2020](#)) scales. We adopt an empirical approach similar to that in [Bluck et al. \(2020\)](#), who tested the validity of this approximation

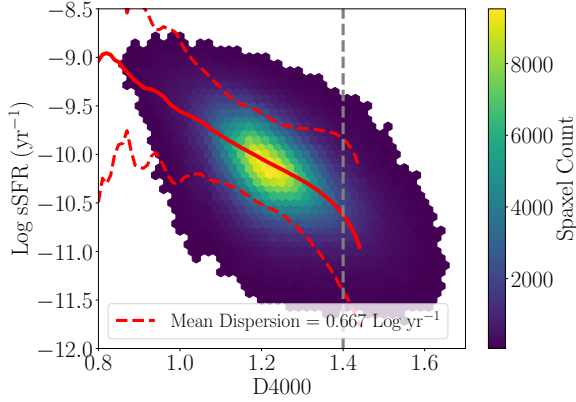


Figure 3. The sSFR-D4000 distribution for all star-forming spaxels in MaNGA (shown as a density hexbin). The median sSFR value in each D4000 bin is shown as red line out to D4000=1.45; this value is used to approximate Σ_{SFR} based on D4000 for spaxels which do not meet the star-forming criteria. The standard deviation of sSFR within each bin is shown as a red dashed line. The median sSFR value steeply changes at high D4000, leading to vary different sSFR values in relatively close D4000 bins. We therefore only use the D4000-sSFR calibration when D4000<1.4 (vertical dashed line).

in the MaNGA PIPE3D data products. For bins of D4000 we compute a median sSFR value based on all star-forming spaxels (using our previous criteria). For any spaxel that does not meet our star-forming criteria, either due to low signal-to-noise or AGN contamination based on the BPT cut, we assign the median sSFR from the closest D4000 bin, and convert that to Σ_{SFR} by multiplying sSFR and Σ_{\star} . Figure 3 displays the complete sSFR-D4000 distribution for star-forming spaxels in MaNGA along with a red line showing the median sSFR value, up to D4000=1.45, used to approximate Σ_{SFR} when a spaxel is not star forming.

Spaxels with D4000>1.45 are generally quenched and therefore the sSFR-D4000 relation is no longer viable (Bluck et al. 2020). As can be seen from Figure 3, the D4000-sSFR relation turns steeply downwards at D4000>1.4. We therefore only estimate Σ_{SFR} from D4000 when D4000<1.4, which represents a slightly stricter cut than that used in Bluck et al. (2020). Table 1 provides the increased spaxel count when both H α - and D4000- Σ_{SFR} values are employed. Of the 13,046 spaxels with CO S/N>3, now 78.8% of spaxels have measurable Σ_{SFR} , almost doubled from the 44.5% of our previous criteria. 9195-3702 and 8450-6102, despite having a considerable number of spaxels with CO S/N>3, still have less than 10 spaxels of overlap between good CO and Σ_{SFR} measurements. These two galaxies are thus excluded from individual galaxy analysis later in this work, along with the other four galaxies previously mentioned. Thus we have 25 galaxies which can be studied on an individual basis, and we limit our studies to these 25 for the rest of the work. Multiple tests are performed to check how using D4000 approximated Σ_{SFR} might impact our results, details of which are included in Appendix C. Adopting this method of measuring Σ_{SFR} sacrifices accuracy for completeness in our analysis; to assess how this will impact our results we repeat key parts of our analysis using only H α - Σ_{SFR} (for galaxies where that is possible). Unless specified otherwise, for the rest of this work Σ_{SFR} and any derived products, use the combined H α +D4000 Σ_{SFR} values for both the merger and isolated sample.

Figure 1 summarizes the various data products from MaNGA and ALMA used within this work for three galaxies from our sample: a post-merger galaxy (top), an interacting pair (middle), and a spectro-

scopic pair (bottom). We display maps of H α - Σ_{SFR} , as well as our combined H α +D4000- Σ_{SFR} map. The middle galaxy is a clear case where we are able to recover a significant number of spaxels using the combined Σ_{SFR} values. In particular, a significant fraction of spaxels in the outskirts of the galaxy are recovered to maximize the spatial coverage of our analysis. Though the middle galaxy demonstrates how the combined H α +D4000- Σ_{SFR} method recovers lower Σ_{SFR} values, the method also recovers AGN dominated spaxels. Thus the main limitation of our analysis becomes the CO signal-to-noise, and the overlap between CO and Σ_{SFR} .

2.3.2 Spaxel Offsets from Resolved Relations

Following Ellison et al. (2020a), we compute offsets from the rKS, rSFMS, and rMGMS to quantify how an individual spaxel may deviate from the average spaxel behaviour. All offsets are computed as the log difference between a spaxel value and the median value of a set of control spaxels that defines the average behaviour, i.e. $\Delta X = \log X - \langle \log X_{\text{control}} \rangle_{\text{median}}$. For example, we define an offset from the SFMS as $\Delta \Sigma_{\text{SFR}}$, with positive $\Delta \Sigma_{\text{SFR}}$ values corresponding to enhanced star formation compared to the control sample. The sample of control spaxels is collected from all DR15 MaNGA spaxels from non-merging galaxies (as classified in Subsection 2.1) with b/a>0.34 (excluding galaxies with inclination greater than 70°) and which are star-forming based on our cuts for the H α - Σ_{SFR} measurements described in Section 2.3.1. All MaNGA Σ_{SFR} values are included, not just ALMaQUEST, such that the requirement for CO detections in ALMaQUEST spaxels does not bias our control spaxel set to higher Σ_{SFR} . Note that we exclude D4000- Σ_{SFR} values from the control sample, given we want to know the difference from the star-forming population that defines the resolved star-forming main sequence. The majority of spaxels on the rSFMS for which we can measure accurate D4000- Σ_{SFR} tend to not meet our star-forming criteria due to low S/N in BPT diagnostic emission lines, rather than being classified as AGN or composite spaxels. Including D4000- Σ_{SFR} in the control would lead to slightly lower $\Delta \Sigma_{\text{SFR}}$ values as a result of the contribution from low S/N spaxels. We have tested whether the inclusion of D4000- Σ_{SFR} in our control would alter any major conclusions of this work, and find our results remain unchanged. From the set of star-forming controls we select a subset that is matched within 0.1 dex Σ_{\star} , 0.1 R/R_e (where R is the inclination corrected galactocentric radius, and the effective radius R_e is the r-band half-light radius from the NSA catalogue), and 0.1 dex M_{\star} of the merger spaxel. The median of this control set defines our “regular” star-forming behaviour. Similar offsets can be determined for the other scaling relations.

An offset from the resolved KS is referred to as ΔSFE ; a value above the KS would have a larger star formation rate given the molecular gas in a spaxel, i.e. an enhancement in the efficiency at which gas is converted to stars. Rather than rely on S/N and BPT cuts to define star-forming spaxels, as was achieved with $\Delta \Sigma_{\text{SFR}}$, we instead make use of the $\Delta \Sigma_{\text{SFR}}$ value to construct the star-forming rKS. The control sample is also limited to galaxies in ALMaQUEST, rather than all of DR15, given Σ_{H_2} is required to compute ΔSFE . Thus the control sample is selected from non-interacting ALMaQUEST galaxies with b/a>0.34, with the additional cut of $-0.5 < \Delta \Sigma_{\text{SFR}} < 0.5$ to select star-forming spaxels. A subset of the control is found by matching to the merger spaxel within 0.1 dex Σ_{H_2} , 0.1 R/R_e , and 0.1 dex M_{\star} .

Using the same control spaxel sample as for ΔSFE , we determine offsets from the rMGMS, referred to as Δf_{H_2} . The control spaxels are again taken from non-interacting ALMaQUEST galaxies and

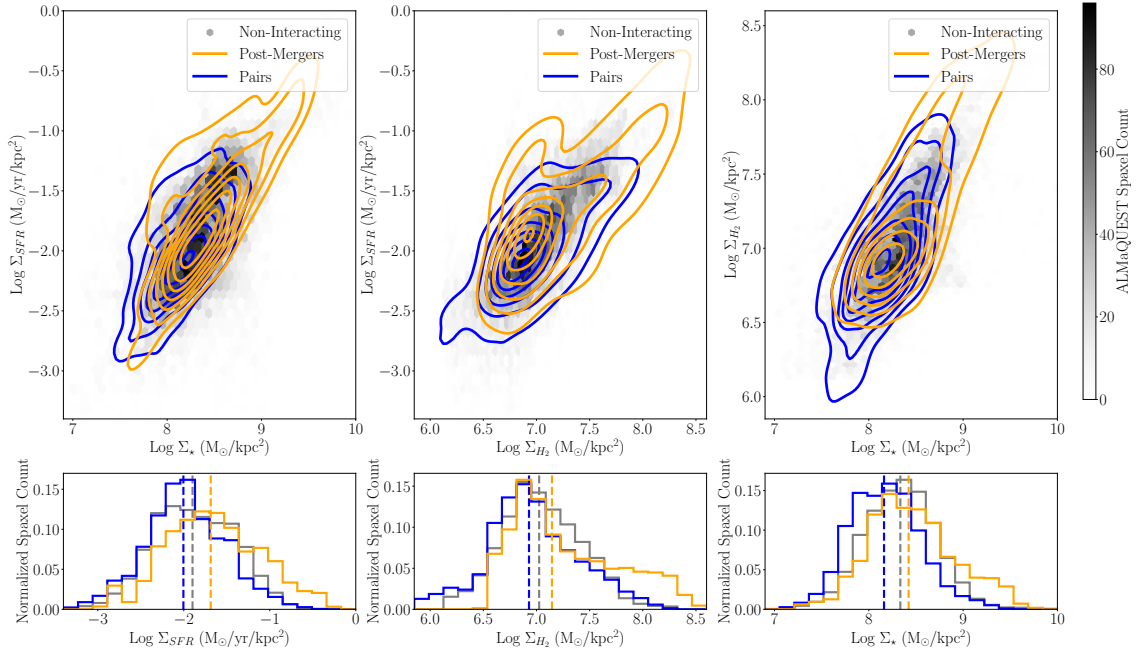


Figure 4. Resolved scaling relations for non-interacting ALMaQUEST galaxies (grey histogram), pairs (blue contours), and post-mergers (orange contours). The rSFMS is shown on the left, the rKS is shown in the middle, and the rMGMS is shown on the right. All measurements required a CO S/N > 3, along with the quality criteria to measure Σ_{SFR} with either H α or D4000 methods as described in Subsection 2.3.1. This results in 22782 isolated spaxels, 7990 pair spaxels, and 4012 post-merger spaxels. Below each histogram distributions of Σ_{SFR} , Σ_{H_2} , and Σ_* are included, separated into non-interacting, post-merger, and pair populations. The median value of each distribution is shown as a horizontal dashed line. Note that the non-interacting ALMaQUEST sample is biased towards higher Σ_{SFR} values resulting from the population of starbursts in the original ALMaQUEST sample (see Subsection 2.3.2 for clarification on how this differs from offset parameter controls). A KS-test reveals that all three populations are distinct from each other in Σ_{SFR} , Σ_{H_2} , and Σ_* . The pair sample has a small offset to lower Σ_{SFR} , Σ_{H_2} , and Σ_* , which is driven by two pair galaxies with uniquely low Σ_* and Σ_{H_2} values (8078-6104 and 8083-12703). But overall all three populations cover a similar range of surface densities.

matched within 0.1 dex Σ_{H_2} , 0.1 R/R_e , and 0.1 dex M_* . Unlike the other two offset metrics, Δf_{H_2} can be computed for any spaxels with CO S/N > 3. Since there is no dependence on whether Σ_{SFR} is measurable, or if measured Σ_{SFR} values overlap with good CO measurements, maps of Δf_{H_2} tend to be more complete than the other two offsets. Maps of offset parameters for the merger sample are available in Appendix D.

One key difference between Ellison et al. (2020a), who first introduced these offset methods, and the methods used here is we do not match control spaxels by metallicity. Limiting our analysis to spaxels with valid metallicity measurements drastically diminishes our total spaxel count, as described in detail in Section 2.2, limiting the spatial coverage of some galaxies and removing three from viable examination entirely. Nonetheless, we have repeated the analysis described in this section with a metallicity control (similar to that used in Ellison et al. 2020a), and find little change in our key results for those galaxies on which this check can be performed (i.e., those with large CO+SFR(H α) overlap).

3 ANALYSIS

3.1 Resolved Scaling Relations

The stellar mass surface density (Σ_*), SFR surface density (Σ_{SFR}), and molecular gas surface density (Σ_{H_2}) are all interconnected in three well established resolved relations: the resolved Kennicutt-Schmidt relation and the resolved molecular gas main sequence, which together drive the resolved star-forming main sequence (Lin et al. 2019; Ellison et al. 2021a; Baker et al. 2022). We investigate these three scaling relations both for merger populations, and for individual galaxies in our merger sample.

Figure 4 compares the resolved scaling relations for post-merger (orange) and pair (blue) galaxies with respect to the relatively isolated galaxies in the rest of ALMaQUEST (grey). Histograms of the Σ_{SFR} , Σ_{H_2} , and Σ_* are provided for context as well. Note that the grey histogram does not represent the control spaxel population used to compute various offset parameters as described in Subsection 2.3.2, rather all spaxels where Σ_{SFR} can be measured for ALMaQUEST. Given the selection of the original ALMaQUEST sample, including a sample of starburst galaxies, the non-interacting spaxels may be biased to high Σ_{SFR} . This is likely why the median Σ_{SFR} for non-interacting galaxies (shown as a dashed line in the Σ_{SFR} histogram) is slightly larger than the median Σ_{SFR} of the pair sample. We perform Kolmogorov-Smirnov (KS) tests between all three samples to

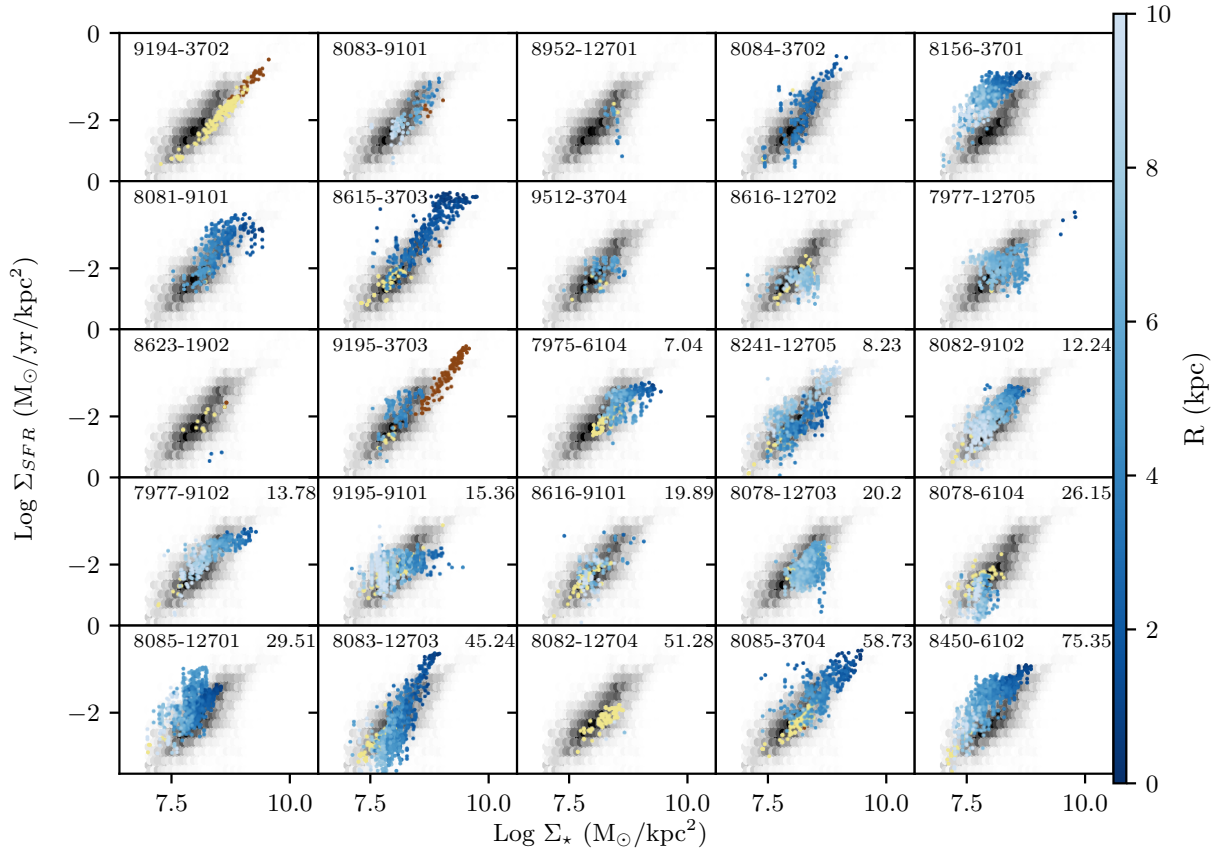


Figure 5. Resolved star-forming main sequence for all merger galaxies, with the MaNGA plate-ifu of the galaxy in the left corner (left blank for post-mergers). Star-forming spaxels are colour-coded by radius, and spaxels with Σ_{SFR} determined by D4000 are yellow (low $\text{H}\alpha$ S/N) or brown (AGN contamination). The non-interacting galaxies in ALMaQUEST are shown as a grey histogram, for reference (including both $\text{H}\alpha$ - Σ_{SFR} and D4000- Σ_{SFR}). Note that there is a diversity of star formation behaviour in the merger sample. Some post-mergers and pairs are significantly offset from the rest of ALMaQUEST. Those which exhibit suppressed star-formation (such as 8241-12705, 7975-6104, and 8078-6104) can be derived from both $\text{H}\alpha$ - and D4000- Σ_{SFR} values, confirming the validity of our combined Σ_{SFR} method.

ascertain whether the pair or post-merger $\Sigma_{\text{SFR}}/\Sigma_{\text{H}_2}/\Sigma_{\star}$ values could be drawn randomly from the non-interacting spaxel sample. We find the probability of this hypothesis to be approximately zero for all three properties ($P_{KS} \approx 0$). The pair sample has a tail towards lower Σ_{H_2} , which seems to be driven by two individual galaxies with uniquely low Σ_{\star} and Σ_{H_2} values (8078-6104 and 8083-12703). The post-merger sample also has a tail towards large Σ_{SFR} , Σ_{H_2} , and Σ_{\star} values, which manifests at the upper end of each scaling relation. Along with the clear lack of post-merger spaxels with $\Sigma_{\text{H}_2} < 6.5 \log M_{\odot}/\text{kpc}^2$, it is clear that our post-merger sample probes regions of heightened SFR and molecular gas properties.

There is significant diversity on a galaxy-per-galaxy basis to consider, as has been seen in other studies (Vulcani et al. 2019; Ellison et al. 2021a; Pessa et al. 2021, Brown et al. in prep). Figure 5 shows the rSFMS for each post-merger and pair galaxy. The star-forming spaxels are colour-coded by radius, while the D4000- Σ_{SFR} are a plain yellow if they did not meet our S/N cuts or brown if they are AGN based on the Kauffmann et al. (2003) criteria. The non-interacting ALMaQUEST spaxels are shown as a grey histogram for comparison (including both $\text{H}\alpha$ - Σ_{SFR} and D4000- Σ_{SFR}). By examining galaxies as individuals we see clear divergence from the spaxels

in non-interacting galaxies, as well as a diversity of behaviour within post-merger and pair classifications. Many mergers show a large population of spaxels above the star-forming main sequence, as is expected if mergers trigger star formation, such as 8156-3701 (1st row, 5th column), 8615-3703 (2nd row, 2nd column), and 8085-12701 (5th row, 1st column). We note that three post-mergers (8084-3702, 8156-3701, 8615-3703) and one pair (8450-6102) were selected from the starburst sample as part of the original ALMaQUEST (ALMA program 2018.1.00541.S, PI: Ellison), which could bias our merger sample towards strongly star-forming galaxies. Yet many spaxels and at times entire mergers are also below the star-forming main sequence, such as 9194-3702 (1st row, 1st column), 7975-6104 (3rd row, 3rd column), and 8078-12703 (4th row, 4th column). In particular, both galaxies with concentrations of “AGN” spaxels as defined by the BPT diagram tend to lie below the non-interacting rSFMS (see 9194-3702 (1st row, 1st column) and 9195-3703 (3rd row, 2nd column)), as has been observed previously with global quantities (Ellison et al. 2016; Leslie et al. 2016; McPartland et al. 2019). This range of enhanced and suppressed star formation rates drives much of the overall scatter of our sample on the global star-forming main sequence (refer back to Figure 2).

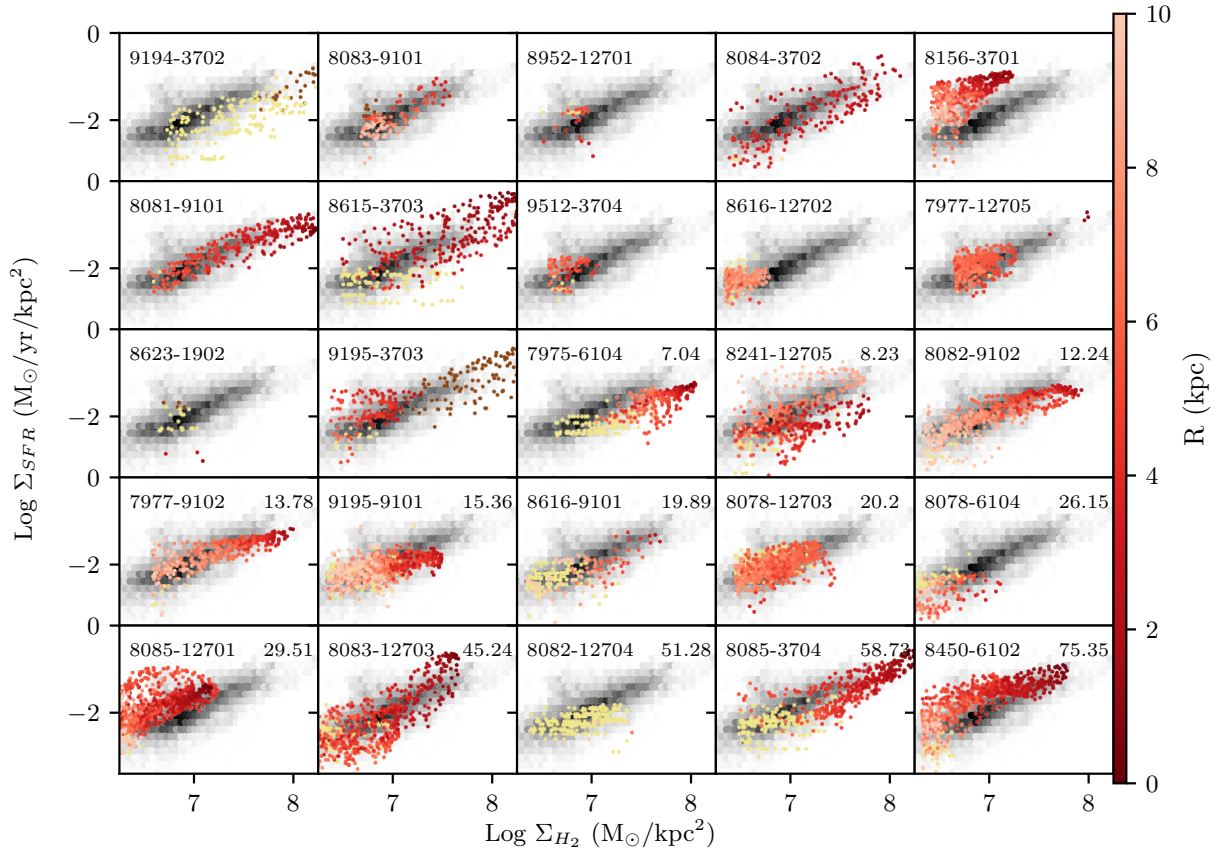


Figure 6. Resolved Kennicutt-Schmidt relation for all merger galaxies, with the MaNGA plate-ifu of the galaxy in the left corner and r_p (kpc) in the right corner (left blank for post-mergers). Star-forming spaxels are red and colour-coded by radius, and spaxels with Σ_{SFR} determined by D4000 are yellow (low $\text{H}\alpha$ S/N) or brown (AGN contamination). The non-interacting galaxies in ALMaQUEST are shown as a grey histogram, for reference, (including both $\text{H}\alpha$ - Σ_{SFR} and D4000- Σ_{SFR}). By examining mergers on an individual basis we see many mergers that are offset, both above and below, the non-interacting rKS.

Mergers present diverse behaviour in the rKS as well, as shown in Figure 6. Many post-mergers and pairs have overall greater scatter in the rKS than the non-interacting sample (see 8615-3703 (2nd row, 2nd column), 8085-12701 (5th row, 1st column), 8083-12703 (5th row, 2nd column)), looking “puffier”; a similar effect as was seen in Ellison et al. (2021a). The increased scatter could represent smaller regions of enhanced SFE in a merger that, on average, has a low or normal global SFE. Note that although D4000- Σ_{SFR} values tend to be lower on the rKS, many still overlap with $\text{H}\alpha$ - Σ_{SFR} spaxels. Spaxels which are classified as “AGN” by a BPT diagram (brown in the figure) tend to exist at larger Σ_{H_2} and Σ_{SFR} values, reflecting their central location in the galaxy and the overall radial dependence of the rKS (smaller radii predominantly fill the upper end of the rKS). However, AGN spaxels at large Σ_{H_2} could also support a scenario where the infall of molecular gas fuels a central AGN. The two largest AGN spaxel populations belonging to post-mergers appears to support such a scenario, though two galaxies alone are not enough to determine if one scenario is more likely than another. Such a query can be further investigated by looking for enhancements in the molecular gas main sequence at high Σ_{H_2} values.

Figure 7 appears to confirm that variations in the rMGMS are the least drastic of the three relations, as was found for non-interacting galaxies by Ellison et al. (2021a). Interestingly, the AGN spaxels

(shown in brown) are not offset to below the rMGMS, as would be implied by the comparatively low gas fractions found for AGN spaxels with MaNGA (Sánchez et al. 2018) and EDGE-CALIFA (Ellison et al. 2021b). Rather the AGN spaxels in the merger sample are comparable to star-forming isolated spaxels, or even enhanced in the case of 9194-3702 (1st row, 1st column) and 9195-3703 (3rd row, 2nd column). What seems to be an inconsistency may stem from the unique nature of the merger stage. Rather than capture central gas depletion triggered by an AGN, as in the isolated galaxies of Ellison et al. (2021b), mergers may have more recently funnelled molecular gas to the galaxy’s centre which has yet to be consumed by the AGN. In the next section we will investigate what drives a merger galaxy to be offset from the resolved scaling relations by comparing spaxel offsets from scaling relations.

3.2 Efficiency vs. Fuel Driven Enhanced Star Formation

We can use maps of spaxel offsets from resolved scaling relations ($\Delta\Sigma_{\text{SFR}}$, ΔSFE , and Δf_{H_2} , as described in Subsection 2.3.2), to discern whether changes in SFE or f_{H_2} drive enhancements in star formation rate. Figure 8 shows the offset maps for an example post-merger galaxy, maps for the entire sample are available in Appendix

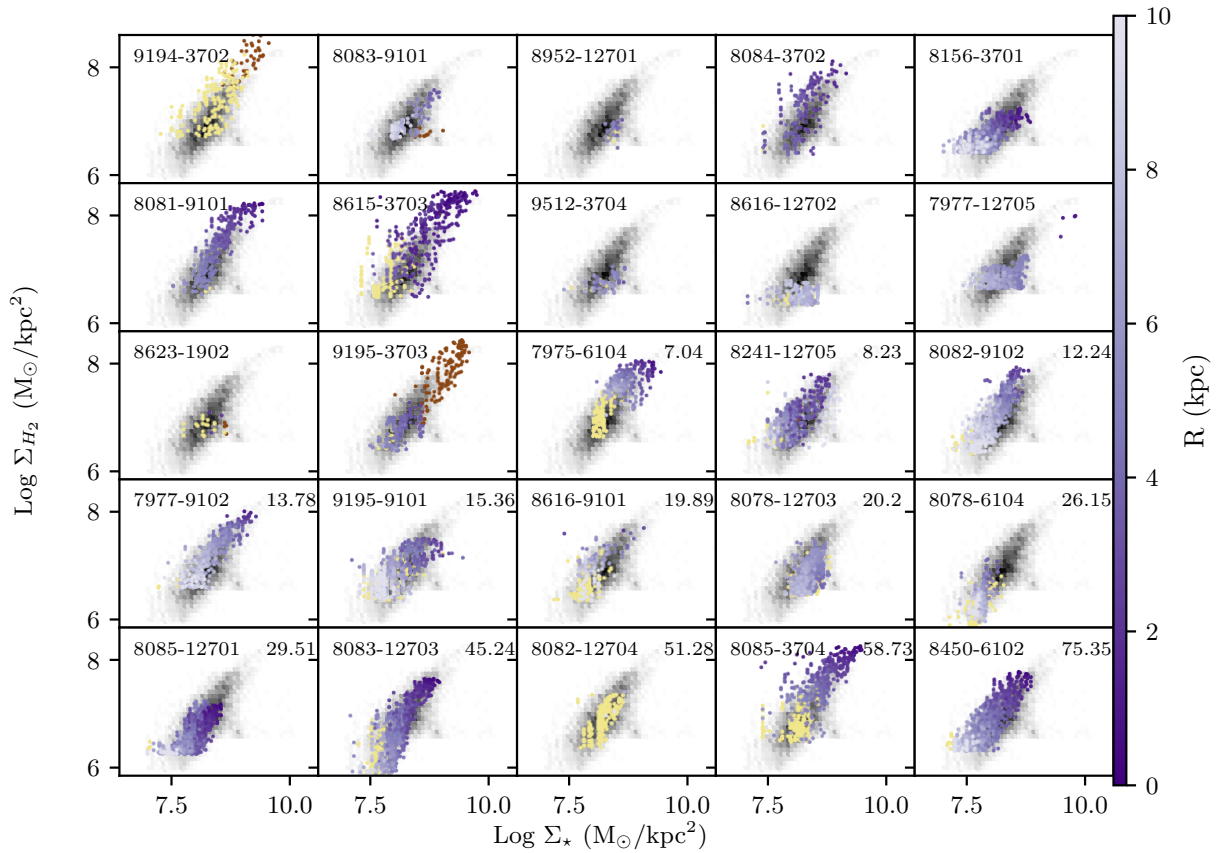


Figure 7. Resolved molecular gas main sequence for all merger galaxies, with the MaNGA plate-i/u of the galaxy in the left corner and r_p (kpc) in the right corner (left blank for post-mergers). Star-forming spaxels are colour-coded purple by radius, and spaxels with Σ_{SFR} determined by D4000 are yellow (low H α S/N) or brown (AGN contamination). The non-interacting galaxies in ALMaQUEST are shown as a grey histogram, for reference. Many merging galaxies have tails at the high mass end of the molecular gas main sequence, at times for AGN spaxels as well (supporting a paradigm where mergers fuel AGN).

D, for which we can attempt to discern whether star formation is driven by enhanced SFE or enhanced f_{H_2} . Star formation in this post-merger is generally enhanced ($\Delta\Sigma_{\text{SFR}} > 0$), as is expected given the average spatial enhancement of post-mergers (see Thorp et al. 2019). That enhancement corresponds to a global enhancement in star formation efficiency (positive ΔSFE). Interestingly, this post-merger mostly has a deficit in molecular gas (negative Δf_{H_2}), with some smaller regions of surplus gas. Figure 8 thus implies that the boost of star formation in this post-merger in particular is predominantly driven by an enhanced efficiency at which gas is converted to stars, not an enhanced amount of gas to fuel that star formation.

From the offset maps alone we can infer some interesting behaviour. Many pair galaxies, for example, have large Δf_{H_2} values along spiral arms (see 9195-9101, 7977-9102, and 8241-12705 in Appendix D). Some pair galaxies have central enhancements in Σ_{H_2} that correspond to a central burst of star formation, such as 9195-3703 and 8078-6104. These two galaxies support a scenario where inflow of molecular gas fuels merger triggered central star formation. Post-merger galaxies 8615-3703 and 8084-3702 have an excess of molecular gas across the galaxy’s surface, rather than a central concentration. Yet that is not a universal scenario; within our sample, 8156-3701 has one of the strongest enhancements in SFR, but has suppressed Σ_{H_2} across the galaxy.

Although the distribution of these offset parameters can reveal interesting results for individual galaxy behaviour, it is difficult to extract general trends for merging and post-merger galaxies from visual examination alone. In particular it is difficult to parse whether enhanced SFE or enhanced Σ_{H_2} drives any merger-triggered star formation. To discern which mechanism is likely more influential over star formation enhancements, we implement an analysis which includes all three offset parameters in a single diagram as pioneered by Ellison et al. (2020a) using ALMaQUEST and Moreno et al. (2021) using simulations.

Figure 9 shows the offsets in star formation efficiency versus the offsets in molecular gas, for all spaxels with enhanced star formation ($\Delta\Sigma_{\text{SFR}} > 0$). We separate the galaxies into three categories: the non-interacting set from ALMaQUEST, pair galaxies, and post-merger galaxies. For these diagrams we plot the line of equality which is used to distinguish an “efficiency driven” and “fuel driven” regime, i.e. where one offset is greater than the other. If a spaxel lies above this line of equality, then $\Delta\text{SFE} > \Delta f_{\text{H}_2}$; if $\Delta\Sigma_{\text{SFR}} > 0$ this would imply enhanced efficiency is prompting the enhanced star formation, more so than the gas fraction. All three galaxy populations have a relatively equal percentage of spaxels in the efficiency driven and fuel driven regime, implying that enhanced star formation is equally driven by enhanced fuel and SFE when all spaxels are examined together. There

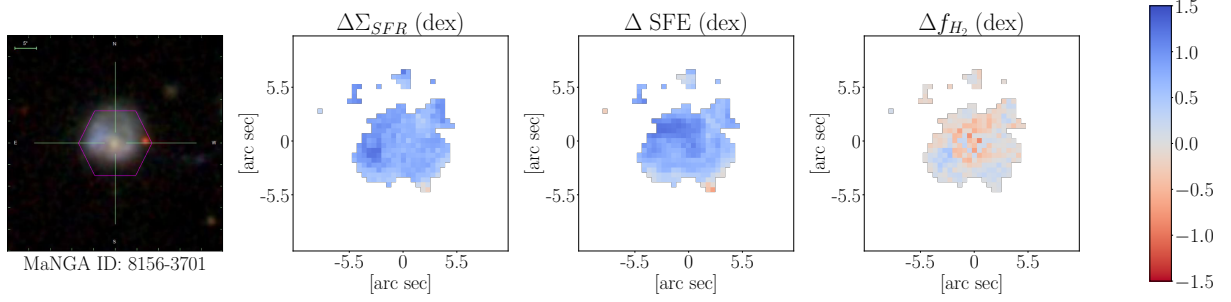


Figure 8. Maps of the offset parameters for an example post-merger galaxy. 1st column: the SDSS *gri*-image of the galaxy, for reference. 2nd column: $\Delta\Sigma_{SFR}$ distribution, with blue representing an enhancement in star formation. 3rd column: ΔSFE distribution, with blue representing enhanced star formation efficiency. 4th column: Δf_{H_2} distribution, with blue representing enhanced gas fraction in a spaxel. The correlation between a uniform enhancement in Σ_{SFR} and SFE, along with the patchy deficits of molecular gas, imply that the star formation in this galaxy is driven by an enhanced efficiency at which gas is converted to stars.

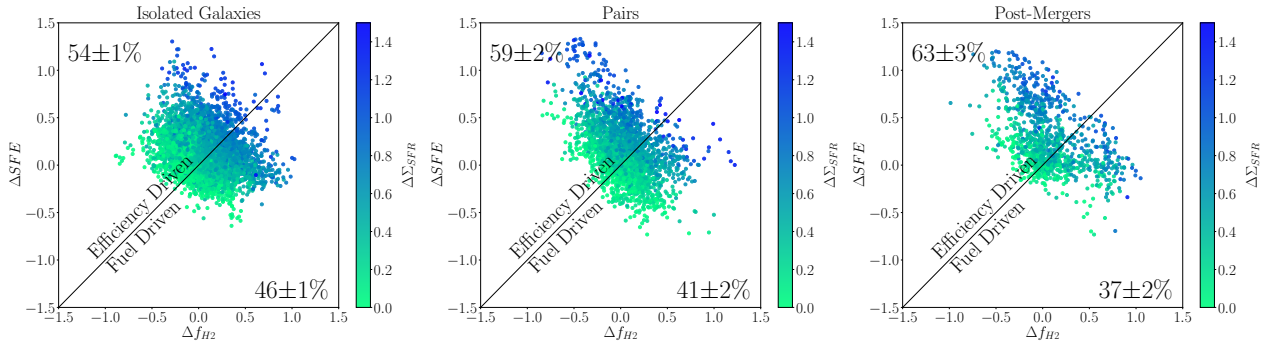


Figure 9. ΔSFE versus Δf_{H_2} for all spaxels that have $\Delta\Sigma_{SFR} > 0$, separated into spaxels which belong to isolated galaxies (left), pair galaxies (middle), and post-merger galaxies (right). Spaxels are colour-coded by $\Delta\Sigma_{SFR}$. The line of equality is shown to delineate the efficiency driven regime (where $\Delta SFE > \Delta f_{H_2}$) and the fuel driven regime (where $\Delta SFE < \Delta f_{H_2}$). The percentage of isolated/pair/post-merger spaxels in each regime is overplotted on the figure, with the uncertainty in the percentage being propagated error of the number of spaxels above/below the line divided by the total number of spaxels. Based on these percentages there is a slight bias towards efficiency driven star formation in post-mergers and pairs (though more so in the former), but other than that the amount of efficiency and fuelled spaxels with enhanced star formation is relatively even.

is a slight bias towards efficiency driven star formation for the post-merger spaxels, with 63% of spaxels in the efficiency driven regime. We remind the reader that the original ALMaQUEST sample includes 11 galaxies that were deliberately selected to be starbursts (Ellison et al. 2020a). Three of these starbursts are in our post-merger sample, one is in the pairs sample, and 12 are in our isolated sample. Since Ellison et al. (2020a) showed that starbursts tend to be dominated by high SFEs, the isolated sample in Figure 9 is not statistically representative of a normal galaxy distribution.

Figure 9 might lead us to believe that enhancements in both SFE and f_{H_2} are equally important for driving SFR enhancements in both post-mergers and pairs. However, in the previous subsection, we found that ensemble spaxel distributions showed considerable diversity when plotted on a galaxy-by-galaxy basis. We now investigate whether the same is true for distributions of offset properties. Figure 10 replicates the combined offset diagram from Figure 9, but for a single post-merger galaxy (the same one that is shown in Figure 8). 96% of spaxels with $\Delta\Sigma_{SFR} > 0$ in this galaxy are in the efficiency driven regime, confirming that the star formation in this galaxy is driven by enhanced SFE as is evident from visually inspecting Figure 8. Figure 10 highlights that whilst the ensemble of spaxels across all galaxies might have a relatively even split between those whose star formation

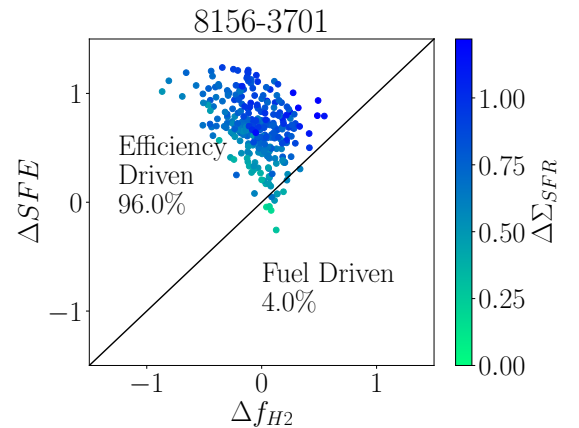


Figure 10. ΔSFE versus Δf_{H_2} for all spaxels with $\Delta\Sigma_{SFR} > 0$ in an example post-merger galaxy (MaNGA plate-ifu = 8156-3701). In this galaxy almost all spaxels are in the efficiency driven regime, as we might expect from examining the distribution of offset parameters in Figure 8.

is enhanced by SFE or gas fraction (Figure 9), individual galaxies may be strongly driven by one process or the other.

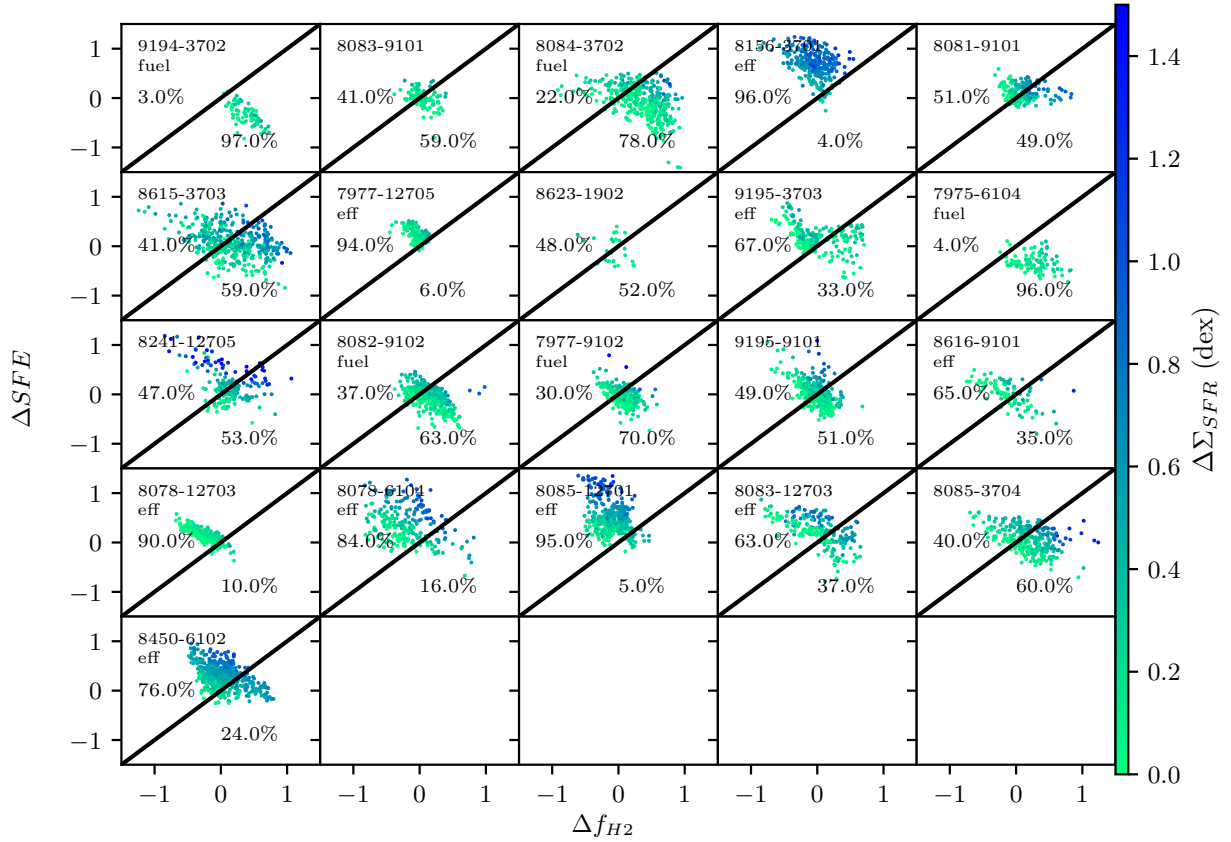


Figure 11. ΔSFE versus Δf_{H_2} for all spaxels with $\Delta \Sigma_{SFR} > 0$ in each post-merger galaxies with more than 20 spaxels with $\Delta \Sigma_{SFR} > 0$, the plate-ifu number of each galaxy is provided in the left corner of every plot. Spaxels are colour-coded by $\Delta \Sigma_{SFR}$. The percentage of spaxels above and below the line of equality are provided as well, which help discern whether the star formation in a galaxy is predominantly driven by enhanced SFE or enhanced f_{H_2} . We label galaxies which are predominantly efficiency driven ($< 40\%$ below the line) and fuel driven ($> 60\%$ above the line) for reference. For some galaxies there is clearly a dominant mechanism driving star formation, but many galaxies have contributions from both efficiency and fuel driven SFR enhancements.

Offset diagrams like that in Figure 10 are provided for all mergers which have more than 20 spaxels where $\Delta \Sigma_{SFR} > 0$ in Figure 11, including the percentage of spaxels in the fuel/efficiency driven regimes. There are cases of both post-merger and pair galaxies that are indisputably driven by a single mechanism, such as 9194-3702 (fuel driven) or 8085-12701 (efficiency driven), but for the majority the dominant star formation driver is less clear. In order to classify the dominance of fuel or efficiency in driving star formation enhancements on a galaxy-by-galaxy basis, we quantify the percentage of spaxels in the fuel/efficiency driven regime of our offset diagrams. If more than 60% of a galaxy’s $\Delta \Sigma_{SFR} > 0$ spaxels are in the fuel-driven regime (i.e., $\Delta f_{H_2} > \Delta SFE$), then we classify the galaxy as “fuel-driven”. If less than 40% of a galaxy’s $\Delta \Sigma_{SFR} > 0$ spaxels are in the fuel-driven regime, then we classify the galaxy as “efficiency driven”. If the percentage of spaxels in the fuel-driven regime is between 40% and 60%, we can assume that enhanced amounts of gas and enhanced SFE are approximately equally contributing to the enhanced star formation. Note that this method of classification gives equal weight to all spaxels, regardless of the strength of star-formation in each spaxel. By doing so our analysis focuses on what mechanism drives star-formation for most regions in a galaxy, not necessarily the mechanism which drives “the most” star-formation.

The fraction of fuel driven spaxels for every merger is listed in Table 2. We calculate this fraction for both our combined Σ_{SFR} values and for the $H\alpha$ - Σ_{SFR} only, although some mergers do not have enough $H\alpha$ - Σ_{SFR} spaxels to meet our criteria. For galaxies which have enough $H\alpha$ - Σ_{SFR} spaxels to measure the fuel-driven fraction, we find adding D4000- Σ_{SFR} to the analysis does not change the classification of the galaxy as fuel or efficiency driven (except for 8616-9101). Interestingly, those galaxies we are only able to analyze with the inclusion of D4000- Σ_{SFR} tend to have large fractions of fuel driven spaxels, i.e. the star formation is driven by an excess of fuel. All four recovered galaxies miss our $H\alpha$ - Σ_{SFR} criteria based on low signal-to-noise, implying that the star formation in these galaxies is truly low (and thus a small or negative ΔSFE is to be expected). Further discussion on how D4000- Σ_{SFR} impacts the fraction of fuel driven spaxels is included in Appendix C, where we find the inclusion of D4000- Σ_{SFR} does not drastically change our results. For both Σ_{SFR} measurement methods there is a relatively similar number of fuel and efficiency driven galaxies, with slightly fewer galaxies driven by neither mechanism. We also consider whether variations in the fraction of fuel driven spaxels could be driven by inaccuracies resulting from using a constant α_{CO} conversion factor. We investigate the error in Σ_{H_2} from using a constant conversion factor, and

Table 2. The fraction of $\Delta\Sigma_{SFR} > 0$ spaxels in the fuel driven regime (i.e., $\Delta f_{H_2} > \Delta SFE$) for each merger with more than 20 $\Delta\Sigma_{SFR} > 0$ spaxels. The fraction of fuel driven spaxels is computed using the combined $H\alpha$ +D4000 Σ_{SFR} , as well as just the $H\alpha$ star formation rates (with appropriate cuts). Note some galaxies do not have fractions computed for $H\alpha$, because they do not have more than 20 spaxels that meet our star-forming cuts. Fractions greater than 0.6, what we consider a fuel driven merger, are coloured blue. Fractions less than 0.4, what we consider an efficiency driven merger, are coloured red. Those between 0.4 and 0.6 are left black, since both mechanisms contribute relatively equally.

plate-ifu	Fraction of Fuel Driven Spaxels	Fraction of Fuel Driven Spaxels ($H\alpha$ only)
9195-3702	-	-
9194-3702	0.97	-
8083-9101	0.59	0.50
8952-12701	-	-
8084-3702	0.78	0.75
8156-3701	0.04	0.04
8081-9101	0.50	0.53
8615-3703	0.60	0.64
9512-3704	-	-
7977-12705	0.06	0.06
8623-1902	0.52	-
8616-12702	-	-
9195-3703	0.33	0.05
7975-6104	0.97	0.97
8241-12705	0.52	0.52
8082-9102	0.64	0.62
7977-9102	0.69	0.68
9195-9101	0.51	0.55
8616-9101	0.34	0.60
8078-12703	0.10	0.14
8078-6104	0.16	0.21
8085-12701	0.05	0.05
8083-12703	0.38	0.39
8082-12704	-	-
8085-3704	0.60	0.67
8450-6102	0.24	0.24

its impact on the fraction of fuel driven spaxels, in Appendix B, and find our results are robust to variations in α_{CO} .

Figure 12 displays the distribution of the fraction of fuel driven spaxels, both for the merger sample as a whole (grey) and the pair (blue) and post-merger (orange) sub-samples. Both the post-merger and pair sample show relatively equal distribution in fuel fraction implying a diversity of star formation drivers throughout the interaction process. There is an intriguing excess of extremely low fuel fractions (below 0.1), compared to the more uniform distribution above a fuel fraction of 0.5, implying that “efficiency driven” mergers have $\Delta SFE > \Delta f_{H_2}$ in most spaxels. However, given only 3 post-mergers are below a fuel fraction of 0.4, this could be the result of small number statistics.

Both observations (Ellison et al. 2013; Patton et al. 2013; Knapen et al. 2015) and simulations (Cox et al. 2008; Torrey et al. 2012; Moreno et al. 2019; Patton et al. 2020) have demonstrated that merger induced star formation peaks at coalescence. Despite the diversity demonstrated in Table 2, it is interesting to note that 2 of the 3 post-mergers with a global $\Delta SFR > 0.5$ are fuel driven enhancements (9194-3702, 8084-3702). We might wonder, then, if there is some correlation between the fraction of fuel driven spaxels and the interaction stage, with the largest fraction of fuel driven spaxels occurring

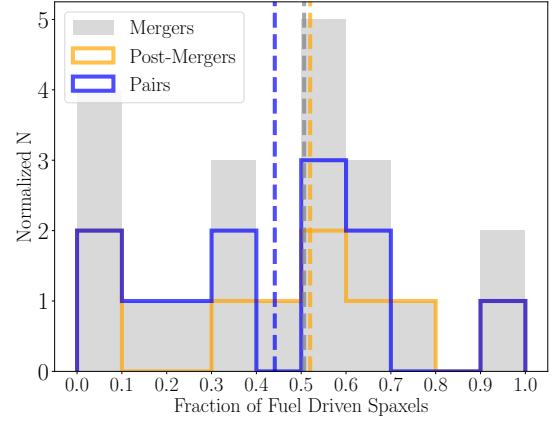


Figure 12. Distributions of the fraction of fuel driven spaxels for the merger sample (grey), along with the pair (blue) and post-merger (orange) sub-samples. The median of each distribution is shown with a vertical dashed line: 0.51 for the entire merger sample, 0.44 for pairs, and 0.52 for post-mergers. The median value of each sub-sample being so similar, and so close to 0.5, confirms that there are an equal number of fuel and efficiency driven mergers.

at coalescence when the star formation is strongest. The higher percentage of efficiency driven galaxies in the pair sample (50% as opposed to 33% in the post-mergers) would agree with a scenario where efficiency driven star-formation becomes less important towards coalescence. Such a correlation would fit with the hypothesis that merger-induced star formation stems from non-axisymmetric structures causing a loss of angular momentum for gas, which then funnels into the centre of the galaxy towards the end of an interaction.

Figure 13 is a visual representation of Table 2, showing the fraction of fuel driven spaxels as a function of projected separation between pairs, with each point colour-coded by global offset from the star-forming main sequence. The post-mergers are shown with a projected separation as arbitrary values below zero, in the grey bar. Figure 13 reveals no clear correlation with the fraction of fuel driven spaxels and the projected separation (Pearson’s correlation coefficient = -0.355). Thus there is no evidence from our sample that the merger stage is strongly linked to whether enhanced star formation is driven by elevated fuel or efficiency. It is important to note that projected separation is not a perfect representation of merger stage due to both uncertainty on whether a galaxy has already completed one or more pericentric passages, as well as projection effects. Morphological signs can serve as an additional indicator for interaction stage given galaxies are most disturbed at first passage and right before coalescence (Lotz et al. 2004, 2008; Hambleton et al. 2011). Unfortunately most of our mergers have some degree of visual disturbance, making it difficult to directly link morphology to a distinct interaction stage (outside of pre- and post-coalescence). We attempt to account for this by highlighting pair galaxies which are connected to their companion by a tidal arm on Figure 13, as a more concrete indicator that first passage has already occurred. Even with this additional category, no trend with merger stage and fraction of fuel driven spaxels arises, further affirming that interaction stage plays a secondary role influencing how star formation is enhanced.

Figure 13 encapsulates one of the main conclusions of this paper: interacting galaxies show a broad diversity of the relative contributions of fuel and efficiency, with no obvious dependence on the merger stage we adopted. This sample suggests that the properties

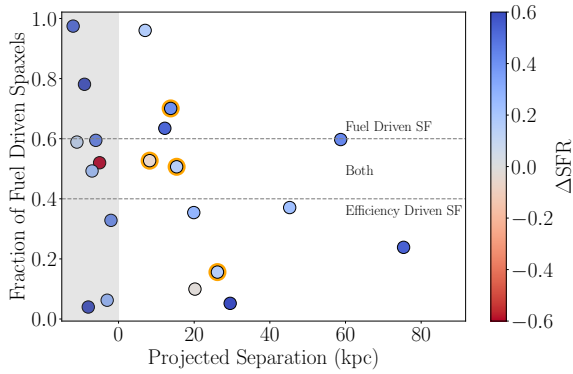


Figure 13. Fraction of fuel driven spaxels as a function of projected separation in kpc, with post-mergers in the grey region (since projected separation cannot be measured without a companion). All points are colour-coded by the galaxy’s global offset from the star-forming main sequence, ΔSFR (bluer points have globally enhanced SFR, red points have globally suppressed SFR, compared with the global SFMS). Note that galaxies with negative ΔSFR can still have regions of enhanced star-formation, which we use to compute a fuel fraction. Pairs that have tidal arms connecting the two galaxies are highlighted with orange. Neither projected separation, nor this secondary morphology characteristic, show any trend with the fraction of fuel driven spaxels.

of the galaxies themselves (e.g. gas fractions, morphologies) as well as the details of the interaction (orbit and mass ratio) play a larger role in how star formation is enhanced. We have checked to see if the fraction of fuel driven spaxels correlates with M_* , M_{H_2} , f_{H_2} , SFR, and ΔSFR , and found only M_{H_2} and f_{H_2} have a Pearson’s correlation coefficient greater than 0.6 (note that f_{H_2} and M_{H_2} are themselves correlated, with a Pearson’s correlation coefficient of 0.69). However, a correlation between the fraction of spaxels driven by enhanced amounts of molecular gas and large gas fractions is not a particularly noteworthy result. More likely it is the combined properties of the galaxy and its companion that drive the diversity of star formation properties observed. Recent simulations have found that mass ratio and orbital geometry can both impact how star formation is powered in mergers (Moreno et al. 2021). It is possible that, with a larger sample, more pronounced correlations with merger stage or integrated galaxy property would emerge, but for this sample such trends are not obvious.

3.3 What drives resolved changes in star formation?

We have shown that, for both pair and post-merger galaxies, either enhanced SFE or enhanced f_{H_2} can drive the subsequent star formation enhancement that results from an interaction. The merger sample is split evenly between galaxies whose star formation driven by SFE, by f_{H_2} , and those equally driven by both. An underlying issue yet to be addressed is how the mechanism which powers star formation relates to the spatial variations in star formation.

Figure 14 displays radial profiles of $\Delta\Sigma_{\text{SFR}}$ for the merger sample separated into distinct categories of efficiency driven, fuel driven, or driven by both based on the fraction of fuel driven spaxels in Table 2 (profiles are additionally colour-coded by the exact fuel fraction computed). By creating radial profiles of offsets in Σ_{SFR} we can investigate whether the fuel fraction we have computed can help explain the diversity of merger radial profiles seen with previous MaNGA studies (i.e., Thorp et al. 2019; Pan et al. 2019; Steffen et al. 2021). A more detailed analysis of merger radial profiles for different

ALMaQUEST data products will be included in Pan et al. (in prep); what is discussed here is simply to assess how our global fuel fraction might relate to variations in Σ_{SFR} already noted by previous works.

The efficiency driven and fuel driven radial profiles in Figure 14 have clearly distinct behaviour. Fuel driven mergers tend to have greater $\Delta\Sigma_{\text{SFR}}$ at small radii, though that does not always lead to a suppression of star formation in the outskirts. Efficiency driven mergers have both greater peaks in $\Delta\Sigma_{\text{SFR}}$ (5 out of 9 surpass 0.5 dex enhancement at one point) and a greater diversity in profile behaviour. Profiles for the efficiency driven mergers can both increase $\Delta\Sigma_{\text{SFR}}$ with radius, decrease $\Delta\Sigma_{\text{SFR}}$ with radius, or have consistent $\Delta\Sigma_{\text{SFR}}$ out to $2R_e$. Thus it is likely a diversity of fuel fraction values could explain some of the diversity of post-merger profiles noted in Thorp et al. (2019). Interestingly, the fuel driven mergers show similar profiles to the starburst $\Delta\Sigma_{\text{SFR}}$ profiles found in Ellison et al. (2020a), despite non-interacting starbursts being primarily driven by enhanced SFE. It is possible that mergers provide one route to a starburst by funneling gas to a centralized starburst, and the resulting SFR enhancement profile is indistinguishable from secular starbursts. Efficiency driven mergers, on the other hand, are more likely to have stronger and continuous SFR enhancements that distinguish them from isolated galaxies of a similar ΔSFR . In the case of the later, the strongest bursts of star formation cannot be driven by enhanced gas reservoirs alone.

There are still issues with applying a single “fuel driven” prescription to what is clearly quite variable on the resolved scale. Simulations of the resolved gas properties of mergers have demonstrated that mergers with overall suppressed star formation can still have appreciable amounts of centralized cold-dense gas (Moreno et al. 2021). We can see this in our handful of fuel-driven mergers that have suppressed star formation beyond $1R_e$, despite centralized boosts in star-formation. It is possible that, though a merger is primarily fuel or efficiency driven, there are regions that deviate from this norm. After all, the mergers which are driven by “both” are lacking any trend in radial profile unlike the other two categories. It is clearly worthwhile to explore how the dominant mechanism might vary within a galaxy.

We attempt to pinpoint spatial variations in the dominant star-forming mechanism by examining the difference between ΔSFE and Δf_{H_2} . The difference between two offset parameters provides a rough approximation of which offset is dominant in an individual spaxel by simply quantifying which is larger. The difference between ΔSFE and Δf_{H_2} is a bit like a fuel fraction for each spaxel, though we note that the number attributed to each has no physical meaning beyond comparing offset values. We can thus construct maps of $\Delta\text{SFE} - \Delta f_{\text{H}_2}$ to demonstrate which mechanism is more important within a certain region of a galaxy. We only consider this for spaxels where $\Delta\Sigma_{\text{SFR}}$, ΔSFE , and Δf_{H_2} are positive, to avoid interpreting the contribution of suppressed SFE or f_{H_2} .

Figure 15 displays maps of $\Delta\text{SFE} - \Delta f_{\text{H}_2}$ for three example galaxies, in conjunction with the ΔSFE vs. Δf_{H_2} diagram colour-coded by $\Delta\text{SFE} - \Delta f_{\text{H}_2}$. Note how the magnitude of $\Delta\text{SFE} - \Delta f_{\text{H}_2}$ scales with distance from the line of equality, where the contribution from SFE and f_{H_2} is equal. Regions where ΔSFE is greater are shown in purple, and regions where Δf_{H_2} is greater are shown in brown. We specifically chose three galaxies that are predominantly efficiency or fuel driven, to demonstrate how this clear-cut classification may break down on a spaxel-per-spaxel basis.

Figure 15 demonstrates that, even within a given galaxy, the dominant driver of enhanced star formation can vary spatially. The first row of Figure 15 shows a post-merger galaxy with a global fuel fraction of 0.33, indicating that SFE is the dominant driver of enhanced star formation. However, a more complicated picture emerges when

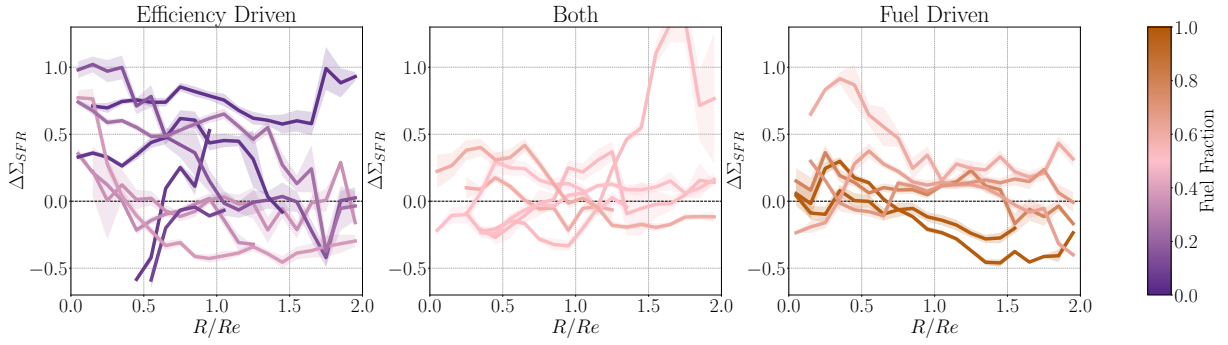


Figure 14. Radial profiles of the median $\Delta\Sigma_{SFR}$ in bins of effective radius for post-merger and pair galaxies included in our analyses, separated into groups of “Efficiency Driven”, “Both”, and “Fuel Driven” based on the fuel fraction value (the second column of Table 2). Each profile is also colour-coded by the fuel fraction. Radial profiles are plotted as a function of the effective radius, with the solid line representing the median in a bin of $0.1 R_e$, and the faded width of the line representing the error on the mean. Efficiency driven mergers tend to have the strongest and most extended enhancements in star formation. Whereas fuel driven mergers are more likely to have centrally concentrated bursts of star formation, likely due to an inflow of gas.

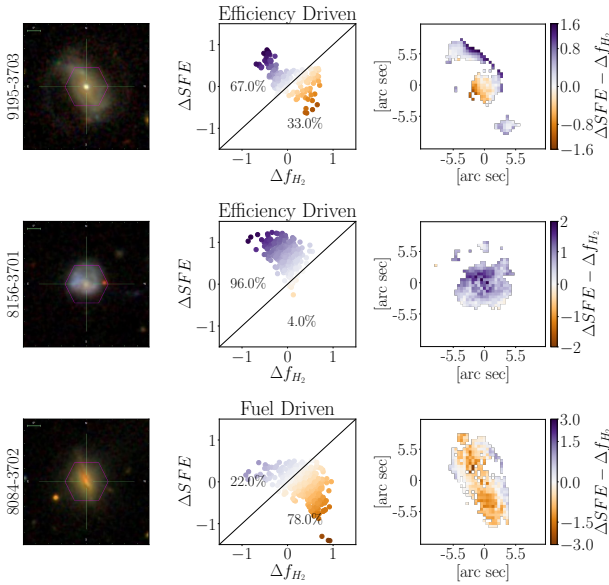


Figure 15. 1st column: *gri*-image of the merger galaxy. 2nd column: ΔSFE versus Δf_{H_2} for all spaxels where $\Delta\Sigma_{SFR} > 0$, colour-coded by $\Delta SFE - \Delta f_{H_2}$. 3rd column: spatially resolved map of $\Delta SFE - \Delta f_{H_2}$ for pixels where all three offset parameters are positive. The colour bars change slightly for each merger, which have different spans of $\Delta SFE - \Delta f_{H_2}$, but zero is always white. Note that $\Delta SFE - \Delta f_{H_2}$ scales with distance from the line of equality shown in the 2nd column. Within each galaxy there is distinct variability in the importance of ΔSFE and Δf_{H_2} , particularly between the centre and outskirts of the galaxy.

we look at the spatially resolved map of $\Delta SFE - \Delta f_{H_2}$ in the right column. Although the extended spiral arms are indeed dominated by enhanced SFE, the core is dominated by enhanced gas fractions. Similar results were found for the Antennae merging galaxies, which had central enhancements in dense gas along with lowered SFE (Bemis & Wilson 2019). By examining maps of $\Delta SFE - \Delta f_{H_2}$ for all mergers (included with offset parameter maps in Appendix D), we find that most of our merger sample follows a similar trend of Δf_{H_2} dominating the central regions of the galaxy.

To quantify whether Δf_{H_2} is more important in the centre of a merging galaxy, we compute a gradient in $\Delta SFE - \Delta f_{H_2}$ for each merger, subtracting the median $\Delta SFE - \Delta f_{H_2}$ within $1R_e$ from the

median where $R > 1R_e$. All but two mergers have a positive gradient (i.e., Δf_{H_2} is more important in the centres than the outskirts), confirming that similar to previous case studies Δf_{H_2} plays a key role in triggering central bursts of star formation. Positive gradients are found both within efficiency driven and fuel driven mergers, with no correlation to the global fraction of fuel driven spaxels (Pearson’s correlation coefficient = -0.19). Efficiency driven mergers have mostly efficiency driven spaxels (positive values in $\Delta SFE - \Delta f_{H_2}$ maps) with fuel driven central starbursts; but given there are more spaxels at large radii than small, those efficiency driven spaxels dominate the percentage of star-forming regions overall. The two mergers with negative gradients, 8156-3701 and 8081-9101, are not unique in their global galaxy properties, but have distinct $\Delta\Sigma_{SFR}$ profiles. 8156-3701 (a post-merger with fuel fraction = 0.04) has $\Delta\Sigma_{SFR} > 0.5$ out to two effective radii, powered by predominantly ΔSFE . In contrast, 8081-9101 (a post-merger fuel fraction = 0.5) has brief suppressions in star formation at the centre and edge of the galaxy, but enhancements ~ 0.25 dex for the majority of the galaxy. Though no substantial result can be derived from two galaxies alone, it is interesting that mergers without central fuel enhancements display two of the most chaotic $\Delta\Sigma_{SFR}$ profiles. However, on average, our sample confirms that central bursts of star formation in mergers require centralized enhancements in gas fraction.

Clearly the consistency of positive gradients in $\Delta SFE - \Delta f_{H_2}$ does not negate further variations between galaxies, as can be seen in the examples from Figure 15 alone. The middle row of Figure 15 shows a post-merger with a negative gradient in $\Delta SFE - \Delta f_{H_2}$. Though star formation in this merger is clearly driven by enhanced SFE (it has a fuel fraction of 0.04), f_{H_2} plays a slightly more important role in the outskirts than in the centre (though ΔSFE is always greater). But even galaxies with a positive gradient, as expected, can have local variations from the norm. The last row of Figure 15 shows a fuel driven post-merger (fuel fraction 0.78) with a positive $\Delta SFE - \Delta f_{H_2}$ gradient. However, regions where $\Delta SFE - \Delta f_{H_2} < 0$ persist out to large radii as well, following a central extended structure within the galaxy. In this case fuel-driven star formation is not limited to the centre of the galaxy (though ΔSFE becomes more important at large radii as well). Such variations are similar to those found in studies of isolated galaxies, where the slope and offset of the rSFMS, rKS, and rMGMS can vary significantly depending on the local galaxy environment (particularly for spiral arms, Pessa et al. 2021). In summary, we find that there is not only considerable diversity from galaxy-to-galaxy in terms of the relative importance of fuel

and efficiency, but even within a given galaxy, different regions show considerable variation.

4 SUMMARY & CONCLUSION

We have presented MaNGA+ALMA CO(1-0) observations of 31 merging galaxies from the ALMaQUEST merger sample in order to study whether interaction-induced star formation is driven primarily by enhancements in SFE or gas fraction. The sample includes 14 post-merger galaxies and 17 pairs with projected separations up to 90 kpc. We compare the rSFMS, rKS, and rMGMS of the merger galaxies to relatively isolated galaxies in the ALMaQUEST survey. Although the ensemble of spaxels in the post-mergers, pairs and isolated galaxies have similar scaling relations (Figure 4), significant variation can be seen when examining the resolved relations for individual mergers (see Figures 5, 6, and 7).

In order to better understand the spatial variations in each merger, we construct maps of offsets from these resolved relations ($\Delta\Sigma_{SFR}$, ΔSFE , and Δf_{H_2}). By directly comparing ΔSFE and Δf_{H_2} for all spaxels with enhanced star formation, we can identify whether the star formation is driven by an enhanced gas reservoir, or an enhanced efficiency at which gas is converted into stars. We find that when all spaxels in all galaxies are considered together, f_{H_2} and SFE contribute equally to enhanced star formation (Figure 9).

However, the approximately equal importance of fuel and efficiency across the entire sample is misleading. When we examine galaxies on an individual basis, a different picture emerges. Some mergers are clearly dominated by either efficiency or fuel driven star formation, with all points lying in one regime of Figure 11. About a third of the merger sample is predominantly efficiency driven, a third is fuel driven, and a third is driven equally by both. We investigate whether the dominant star formation mechanism might be correlated with global galaxy properties (SFR, M_\star , M_{H_2} , f_{H_2} , ΔSFR), and find only an unsurprising correlation with fuel driven star formation and large gas fractions.

The driving star formation mechanism does not depend on the stage of an interaction either. The percentage of fuel driven post-mergers is somewhat more than the percentage of fuel driven pair galaxies. But fuel fraction does not correlate with other indicators of interaction stage, such as projected separation and tidal connections (Figure 13). The progression of the interaction does not lead to clear evolution in the fuel fraction, which implies the unique properties of the progenitors are more influential on which mechanisms powers enhancements in star-formation.

In section 3.3 we investigate how the dominant star-forming mechanism leads to variations on a spatial scale. Radial profiles of $\Delta\Sigma_{SFR}$ for the merger sample are shown in Figure 14, separated into three categories based on fuel fraction. We find that “fuel driven” mergers (with fuel fractions > 0.6) have relatively distinct $\Delta\Sigma_{SFR}$ profiles compared to “efficiency driven” mergers (fuel fraction < 0.4), which often have stronger and more extended $\Delta\Sigma_{SFR}$ enhancements. Thus a range of fuel fractions in mergers could explain the diversity of star formation offset profiles seen in previous merger studies (Thorp et al. 2019; Pan et al. 2019; Steffen et al. 2021).

The range of $\Delta\Sigma_{SFR}$ profiles in these three categories implies more internal variation within a galaxy than a single fuel fraction can capture. Figure 15 demonstrates this variation in the dominant mechanism within a galaxy by presenting 2D maps of $\Delta SFE - \Delta f_{H_2}$, indicating which offset parameter is largest in each spaxel. Even galaxies which are driven predominantly by a single mechanism on a global scale can exhibit internal deviations from the dominant mech-

anism. For example, both efficiency and fuel driven mergers tend to have $\Delta f_{H_2} > \Delta SFE$ in their centre, confirming that enhanced amounts of molecular gas are crucial to merger-induced central starbursts, even if the rest of the galaxy has efficiency driven star formation.

The work presented here is the first to investigate the resolved molecular gas and star formation properties for a relatively large set of mergers spanning a wide range of sSFRs and stages of interaction, with the explicit goal of understanding how gas and star formation evolve with an interaction. Our work adds to the growing evidence that, despite following overall scaling relationships, galaxies are diverse in their details. Moreover, we have shown that in addition to diversity on a global scale (i.e. some mergers have their star formation driven by fuel, others by efficiency), there is significant internal variation on kpc-scales.

ACKNOWLEDGEMENTS

We acknowledge and respect the Lekwungen peoples on whose traditional territories the University of Victoria stands and where the majority of this work was conducted. We strive to honour the Songhees, Esquimalt, and WSÁNEĆ peoples who were the first astronomers of this land and whose continued stewardship is crucial to its preservation.

MDT thanks Jorge Moreno, Shoshannah Byrne-Mamahit, Salvatore Quai, Robert Bickley, Scott Wilkinson and Joanna Woo for discussion throughout the creation of this work, as well as William Baker and Fangting Yuan for key editorial remarks. SLE and DRP gratefully acknowledges NSERC of Canada for Discovery Grants which helped to fund this research. HAP acknowledges support by the Ministry of Science and Technology of Taiwan under grant 110-2112-M-032-020-MY3. SLE, MDT, LL and HAP also gratefully acknowledge grant MOST 107-2119-M-001-024 and 108-2628-M-001-001-MY3 for travel funding that facilitated both the ALMA data reduction and analysis of ALMaQUEST survey.

This paper makes use of the following ALMA data: ADS/JAO.ALMA#2015.1.01225.S, ADS/JAO.ALMA#2017.1.01093.S, ADS/JAO.ALMA#2018.1.00558.S, ADS/JAO.ALMA#2018.1.00541.S, ADS/JAO.ALMA#2019.1.00260.S. ALMA is a partnership of ESO (representing its member states), NSF (USA) and NINS (Japan), together with NRC (Canada), MOST and ASIAA (Taiwan), and KASI (Republic of Korea), in cooperation with the Republic of Chile. The Joint ALMA Observatory is operated by ESO, AUI/NRAO and NAOJ. The National Radio Astronomy Observatory is a facility of the National Science Foundation operated under cooperative agreement by Associated Universities, Inc.

Funding for the Sloan Digital Sky Survey IV has been provided by the Alfred P. Sloan Foundation, the U.S. Department of Energy Office of Science, and the Participating Institutions. SDSS-IV acknowledges support and resources from the Center for High-Performance Computing at the University of Utah. The SDSS web site is www.sdss.org. SDSSIV is managed by the Astrophysical Research Consortium for the Participating Institutions of the SDSS Collaboration including the Brazilian Participation Group, the Carnegie Institution for Science, Carnegie Mellon University, the Chilean Participation Group, the French Participation Group, Harvard-Smithsonian Center for Astrophysics, Instituto de Astrofísica de Canarias, The Johns Hopkins University, Kavli Institute for the Physics and Mathematics of the Universe (IPMU) / University of Tokyo, Lawrence Berkeley National Laboratory, Leibniz Institut für Astrophysik Potsdam (AIP), Max-

Planck-Institut für Astronomie (MPIA Heidelberg), Max-Planck-Institut für Astrophysik (MPA Garching), Max-Planck-Institut für Extraterrestrische Physik (MPE), National Astronomical Observatory of China, New Mexico State University, New York University, University of Notre Dame, Observatório Nacional / MCTI, The Ohio State University, Pennsylvania State University, Shanghai Astronomical Observatory, United Kingdom Participation Group, Universidad Nacional Autónoma de México, University of Arizona, University of Colorado Boulder, University of Oxford, University of Portsmouth, University of Utah, University of Virginia, University of Washington, University of Wisconsin, Vanderbilt University, and Yale University.

DATA AVAILABILITY

The MaNGA data cubes used in this work are publicly available at <https://www.sdss.org/dr15/>. The ALMA data used in this work are publicly available after the standard one year proprietary period via the ALMA archive: <http://almascience.nrao.edu/aq/>.

REFERENCES

- Accurso G., et al., 2017, *Monthly Notices of the Royal Astronomical Society*, 470, 4750
- Allen J. T., et al., 2015, *Monthly Notices of the Royal Astronomical Society*, 446, 1567
- Baker W. M., Maiolino R., Bluck A. F. L., Lin L., Ellison S. L., Belfiore F., Pan H.-A., Thorp M., 2022, *Monthly Notices of the Royal Astronomical Society*, 510, 3622
- Baldwin J. A., Phillips M. M., Terlevich R., 1981, *Publications of the Astronomical Society of the Pacific*, 93, 5
- Barnes J. E., Hernquist L. E., 1991, *The Astrophysical Journal*, 370, L65
- Barrera-Ballesteros J. K., et al., 2015, *Astronomy & Astrophysics*, 579, A45
- Barrera-Ballesteros J. K., et al., 2021, *Monthly Notices of the Royal Astronomical Society*, 18, 1
- Barton Gillespie E. B., Geller M. J., Kenyon S. J., 2003, *The Astrophysical Journal*, 582, 668
- Bemis A., Wilson C. D., 2019, *The Astronomical Journal*, 157, 18
- Bickley R. W., Ellison S. L., Patton D. R., Bottrell C., Gwyn S., Hudson M. J., 2022, *Monthly Notices of the Royal Astronomical Society*, 514, 3294
- Bigiel F., Leroy A., Walter F., Brinks E., De Blok W. J. G., Madore B., Thornley M. D., 2008, *The Astronomical Journal*, 136, 2846
- Bluck A., Maiolino R., Sánchez S., Ellison S., Thorp M., Piotrowska J., Teimoorinia H., Bundy K., 2020, *Monthly Notices of the Royal Astronomical Society*, 492, 96
- Bolatto A. D., Wolfire M., Leroy A. K., 2013, *Annual Review of Astronomy and Astrophysics*, 51, 207
- Bolatto A. D., et al., 2017, *The Astrophysical Journal*, 846, 159
- Bournaud F., et al., 2011, *The Astrophysical Journal*, 730, 4
- Braine J., Combes F., 1992, *Astronomy & Astrophysics*, 269, 7
- Brinchmann J., Charlot S., White S. D. M., Tremonti C., Kauffmann G., Heckman T., Brinkmann J., 2004, *Monthly Notices of the Royal Astronomical Society*, 351, 1151
- Bundy K., et al., 2015, *The Astrophysical Journal*, 798, 7
- Cano-Díaz M., et al., 2016, *The Astrophysical Journal*, 821, L26
- Cardelli J. A., Clayton G. C., Mathis J. S., 1989, *The Astrophysical Journal*, 345, 245
- Casasola V., Bettoni D., Galletta G., 2004, *Astronomy & Astrophysics*, 422, 941
- Chown R., et al., 2019, *Monthly Notices of the Royal Astronomical Society*, 484, 5192
- Colombo D., et al., 2018, *Monthly Notices of the Royal Astronomical Society*, 475, 1791
- Cox T. J., Jonsson P., Primack J. R., Somerville R. S., 2006, *Monthly Notices of the Royal Astronomical Society*, 373, 1013
- Cox T. J., Jonsson P., Somerville R. S., Primack J. R., Dekel A., 2008, *Monthly Notices of the Royal Astronomical Society*, 384, 386
- D’Onghia E., Vogelsberger M., Faucher-Giguere C.-A., Hernquist L., 2010, *The Astrophysical Journal*, 725, 353
- Di Matteo P., Combes F., Melchior A. L., Semelin B., 2007, *Astronomy & Astrophysics*, 468, 61
- Díaz Trigo M., Carpenter J., Maude L., Miura R., Plunkett A., 2019, *ALMA Cycle 7 Proposer’s Guide*, 2019, [doi:10.5281/zenodo.4511962](https://doi.org/10.5281/zenodo.4511962)
- Ellison S. L., Patton D. R., Simard L., McConnachie A. W., 2008, *The Astronomical Journal*, 135, 1877
- Ellison S. L., Mendel J. T., Patton D. R., Scudder J. M., 2013, *Monthly Notices of the Royal Astronomical Society*, 435, 3627
- Ellison S. L., Teimoorinia H., Rosario D. J., Mendel J. T., 2016, *MNRAS*, 458, 34
- Ellison S. L., Catinella B., Cortese L., 2018, *Monthly Notices of the Royal Astronomical Society*, 478, 3447
- Ellison S. L., Thorp M. D., Pan H.-A., Lin L., Scudder J. M., Bluck A. F. L., Sánchez S. F., Sargent M., 2020a, *Monthly Notices of the Royal Astronomical Society*, 492, 6027
- Ellison S., et al., 2020b, *Monthly Notices of the Royal Astronomical Society*, 493, L39
- Ellison S. L., Lin L., Thorp M. D., Pan H.-A., Scudder J. M., Sánchez S. F., Bluck A. F. L., Maiolino R., 2021a, *Monthly Notices of the Royal Astronomical Society*, 501, 4777
- Ellison S. L., et al., 2021b, *MNRAS*, 505, L46
- Fensch J., et al., 2017, *Monthly Notices of the Royal Astronomical Society*, 465, 1934
- Gallagher M. J., et al., 2018, *The Astrophysical Journal*, 858, 90
- González Delgado R. M., et al., 2016, *Astronomy & Astrophysics*, 590
- Hambleton K. M., Gibson B. K., Brook C. B., Stinson G. S., Conselice C. J., Bailin J., Couchman H., Wadsley J., 2011, *Monthly Notices of the Royal Astronomical Society*, 418, 801
- Hani M. H., Gosain H., Ellison S. L., Patton D. R., Torrey P., 2020, *Monthly Notices of the Royal Astronomical Society*, 493, 3716
- Hopkins P. F., Cox T. J., Hernquist L., Narayanan D., Hayward C. C., Murray N., 2013, *Monthly Notices of the Royal Astronomical Society*, 430, 1901
- Huchtmeier W. K., Petrosian A., Krishna G., McLean B., Kunth D., 2008, *Astronomy & Astrophysics*, 492, 367
- Iono D., Yun M. S., Mihos J. C., 2004, *The Astrophysical Journal*, 616, 199
- Jiménez-Donaire M. J., et al., 2019, *The Astrophysical Journal*, 880, 127
- Kauffmann G., et al., 2003, *Monthly Notices of the Royal Astronomical Society*, 346, 1055
- Kennicutt R. C., 1989, *The Astrophysical Journal*, 344, 685
- Kennicutt R. C., Keel W. C., Van Der Hulst J. M., Hummel E., Roettiger K. A., 1987, *The Astronomical Journal*, 93, 1011
- Kennicutt R. C., Tamblyn P., Congdon C. W., 1994, *Astrophysical Journal*, 435, 22
- Knapen J. H., James P. A., 2009, *The Astrophysical Journal*, 698, 1437
- Knapen J. H., Cisternas M., Querejeta M., 2015, *Monthly Notices of the Royal Astronomical Society*, 454, 1742
- Lambas D. G., Alonso S., Mesa V., O’Mill A. L., 2012, *Astronomy & Astrophysics*, 539, A45
- Larson R. B., Tinsley B. M., 1978, *The Astrophysical Journal*, 219, 46
- Law D. R., et al., 2015, *The Astronomical Journal*, 150, 19
- Leroy A. K., Walter F., Brinks E., Bigiel F., De Blok W. J. G., Madore B., Thornley M. D., 2008, *The Astronomical Journal*, 136, 2782
- Leroy A. K., et al., 2013, *The Astronomical Journal*, 146, 19
- Leroy A. K., et al., 2021, *The Astrophysical Journal Supplement Series*, 257, 61
- Leslie S. K., Kewley L. J., Sanders D. B., Lee N., 2016, *MNRAS*, 455, 82
- Lin L., et al., 2007, *The Astrophysical Journal*, 660, 51
- Lin L., et al., 2017, *The Astrophysical Journal*, 851, 18
- Lin L., et al., 2019, *Astrophysical Journal Letters*, 884
- Lin L., et al., 2020, *The Astrophysical Journal*, 903, 19
- Lotz J. M., Primack J., Madau P., 2004, *The Astronomical Journal*, 128, 163
- Lotz J. M., Jonsson P., Cox T., Primack J. R., 2008, *Monthly Notices of the Royal Astronomical Society*, 391, 1137
- McMullin J. P., Waters B., Schiebel D., Young W., Golap K., 2007, in *As-*

tronomical Data Analysis Software and Systems XVI. p. 127, <http://casa.nrao.edu>

McPartland C., Sanders D. B., Kewley L. J., Leslie S. K., 2019, *Monthly Notices of the Royal Astronomical Society: Letters*, 482, L129

Mihos J. C., Hernquist L., 1996, *The Astrophysical Journal*, 464, 641

Moreno J., Torrey P., Ellison S. L., Patton D. R., Bluck A. F., Bansal G., Hernquist L., 2015, *Monthly Notices of the Royal Astronomical Society*, 448, 1107

Moreno J., et al., 2019, *Monthly Notices of the Royal Astronomical Society*, 485, 1320

Moreno J., et al., 2021, *Monthly Notices of the Royal Astronomical Society*, 503, 3113

Narayanan D., Krumholz M. R., Ostriker E. C., Hernquist L., 2012, *Monthly Notices of the Royal Astronomical Society*, 421, 3127

Nikolic B., Cullen H., Alexander P., 2004, *Monthly Notices of the Royal Astronomical Society*, 355, 874

Pan H.-A., et al., 2018, *The Astrophysical Journal*, 868, 132

Pan H.-A., et al., 2019, *The Astrophysical Journal*, 881, 119

Patton D. R., Torrey P., Ellison S. L., Mendel J. T., Scudder J. M., 2013, *Monthly Notices of the Royal Astronomical Society: Letters*, 433, 59

Patton D. R., Qamar F. D., Ellison S. L., Bluck A. F. L., Simard L., Mendel J. T., Moreno J., Torrey P., 2016, *Monthly Notices of the Royal Astronomical Society*, 461, 2589

Patton D. R., et al., 2020, *Monthly Notices of the Royal Astronomical Society*, 494, 4969

Perez J., Michel-Dansac L., Tissera P., 2011, *Monthly Notices of the Royal Astronomical Society*, 417, 580

Pessa I., et al., 2021, *A&A*, 650, A134

Pettini M., Pagel B. E. J., 2004, *Monthly Notices of the Royal Astronomical Society*, 348, L59

Querejeta M., et al., 2021, *A&A*, 656, A133

Salpeter E. E., 1955, *The Astrophysical Journal*, 121, 161

Sánchez S. F., et al., 2012, *Astronomy & Astrophysics*, 538, A8

Sánchez S. F., et al., 2013, *Astronomy & Astrophysics*, 554, A58

Sánchez S. F., et al., 2016a, *Revista Mexicana de Astronomía y Astrofísica*, 52, 21

Sánchez S. F., et al., 2016b, *Revista Mexicana de Astronomía y Astrofísica*, 52, 171

Sánchez S. F., et al., 2018, *Revista Mexicana de Astronomía y Astrofísica*, 54, 217

Schmidt M., 1959, *The Astrophysical Journal*, 129, 243

Schruba A., et al., 2011, *The Astronomical Journal*, 142, 37

Scudder J. M., Ellison S. L., Torrey P., Patton D. R., Mendel J. T., 2012, *Monthly Notices of the Royal Astronomical Society*, 426, 549

Scudder J. M., Ellison S. L., Momjian E., Rosenberg J. L., Torrey P., Patton D. R., Fertig D., Mendel J. T., 2015, *Monthly Notices of the Royal Astronomical Society*, 449, 3719

Spindler A., et al., 2018, *Monthly Notices of the Royal Astronomical Society*, 476, 580

Steffen J. L., Fu H., Comerford J. M., Dai Y. S., Feng S., Gross A. C., Xue R., 2021, *The Astrophysical Journal*, 909, 13

Strauss M. A., Weinberg D. H., Lupton R. H., Narayanan V. K., 2002, *The Astronomical Journal*, 124, 1810

Sun J., et al., 2020, *The Astrophysical Journal*, 892, 28

Thorp M., Ellison S., Simard L., Sánchez S., Antonio B., 2019, *Monthly Notices of the Royal Astronomical Society: Letters*, 482, L55

Tomicić N., et al., 2018, *The Astrophysical Journal Letters*, 869, L38

Torrey P., Cox T. J., Kewley L., Hernquist L., 2012, *The Astrophysical Journal*, 746, 108

Usero A., et al., 2015, *The Astronomical Journal*, 150, 115

Utomo D., et al., 2017, *The Astrophysical Journal*, 849, 16

Violino G., Ellison S. L., Sargent M., Coppin K. E. K., Scudder J. M., Mendel J. T., Saintonge A., 2018, *Monthly Notices of the Royal Astronomical Society*, 476, 2591

Vulcani B., et al., 2019, *Monthly Notices of the Royal Astronomical Society*, 488, 1597

Wang E., Lilly S. J., Pezzulli G., Matthee J., 2019, *The Astrophysical Journal*, 877, 132

Wong T., et al., 2013, *The Astrophysical Journal Letters*, 777

Woods D. F., Geller M. J., Kurtz M. J., Westra E., Fabricant D. G., Dell’Antonio I., 2010, *The Astronomical Journal*, 139, 1857

APPENDIX A: ALMAQUEST - MERGER SET

Included in figure A1–A5 are data product maps for the ALMAQUEST merger set. Post-mergers are shown first, followed by pairs in order of increasing pair separation. All 31 mergers are included, even the 6 galaxies with insufficient overlap between CO $S/N > 3$ and $H\alpha + D4000 - \Sigma_{\text{SFR}}$ measurements which are excluded from individual galaxy analysis. Data products include, from left to right: the SDSS *gri*-image, inclination corrected stellar mass surface density (from PIPE3D), inclination corrected molecular gas surface density (computed from CO luminosity), inclination corrected star formation rate surface density (computed from $H\alpha$ luminosity), inclination corrected star formation rate surface density (computed from $H\alpha$ luminosity and sSFR-D4000 fit), molecular gas fraction ($\Sigma_{\text{H}_2}/\Sigma_{\star}$), and star formation efficiency ($\Sigma_{\text{SFR}}/\Sigma_{\text{H}_2}$).

APPENDIX B: METALLICITY DEPENDENT CO CONVERSION FACTOR

Throughout this work we elect to use a constant α_{CO} rather than a metallicity dependent one. This is highly beneficial to our analysis in that we can include spaxels which do not meet the requirements to measure accurate gas-phase metallicities (requiring high signal-to-noise in multiple emission lines). As a result our Σ_{H_2} measurements will be imperfect, leading to the possibility that variations ΔSFE and Δf_{H_2} (both of which require Σ_{H_2}) could be the result of inaccuracies in α_{CO} . Depending on the degree of that inaccuracy this could sully our final conclusions concerning the role enhanced efficiency and fuel play in increasing star formation activity.

Though we cannot compute a metallicity dependent α_{CO} ($\alpha_{\text{CO, met}}$ from here on) for every spaxel, we can characterize the change in Σ_{H_2} for spaxels where $\alpha_{\text{CO, met}}$ is measurable. We compute a $\alpha_{\text{CO, met}}$ for all spaxels that are star-forming based on the criteria described in Subsection 2.3.1, for which we can also measure the gas phase metallicity using the O3N2 calibration of Pettini & Pagel (2004). We set $\alpha_{\text{CO, met}} = 4.35 \times Z'^{-1.6} (M_{\odot} (\text{K km/s pc}^2)^{-1})$ where Z' is the metallicity normalized to solar metallicity ($Z' = 10^{\text{PP04}_{\text{O3N2}} - 8.69}$) (Sun et al. 2020). We find the median difference between Σ_{H_2} and $\Sigma_{\text{H}_2, \text{met}}$ to be -0.068 dex, with a standard deviation of 0.124 dex. If we want to be conservative, we can say that Δf_{H_2} and ΔSFE both have an uncertainty of 2σ on the difference in Σ_{H_2} , or 0.248 dex. Figure B1 is a replication of Figure 11, with a grey bar representing 0.248 dex of uncertainty; points within this range could change from fuel to efficiency driven, or vice versa, if one switched from a constant to a metallicity dependent α_{CO} . We can thus exclude spaxels within this grey bar from our calculation of the fuel fraction to achieve a value that is independent of variations in α_{CO} . By excluding borderline spaxels, most galaxies tend to be more “fuel” or “efficiency” driven.

Figure B2 directly compares the original fuel fraction, using a constant α_{CO} , to this new one which incorporates error from not using $\alpha_{\text{CO, met}}$. Ideally all points would be along the line of equality, confirming that the fraction of fuel driven spaxels does not change. Instead galaxies which are fuel driven become more fuel driven, rising above the line of equality, and galaxies which are efficiency driven become more efficiency driven. As a result very few galaxies change whether we would consider them “efficiency” or “fuel” driven. We

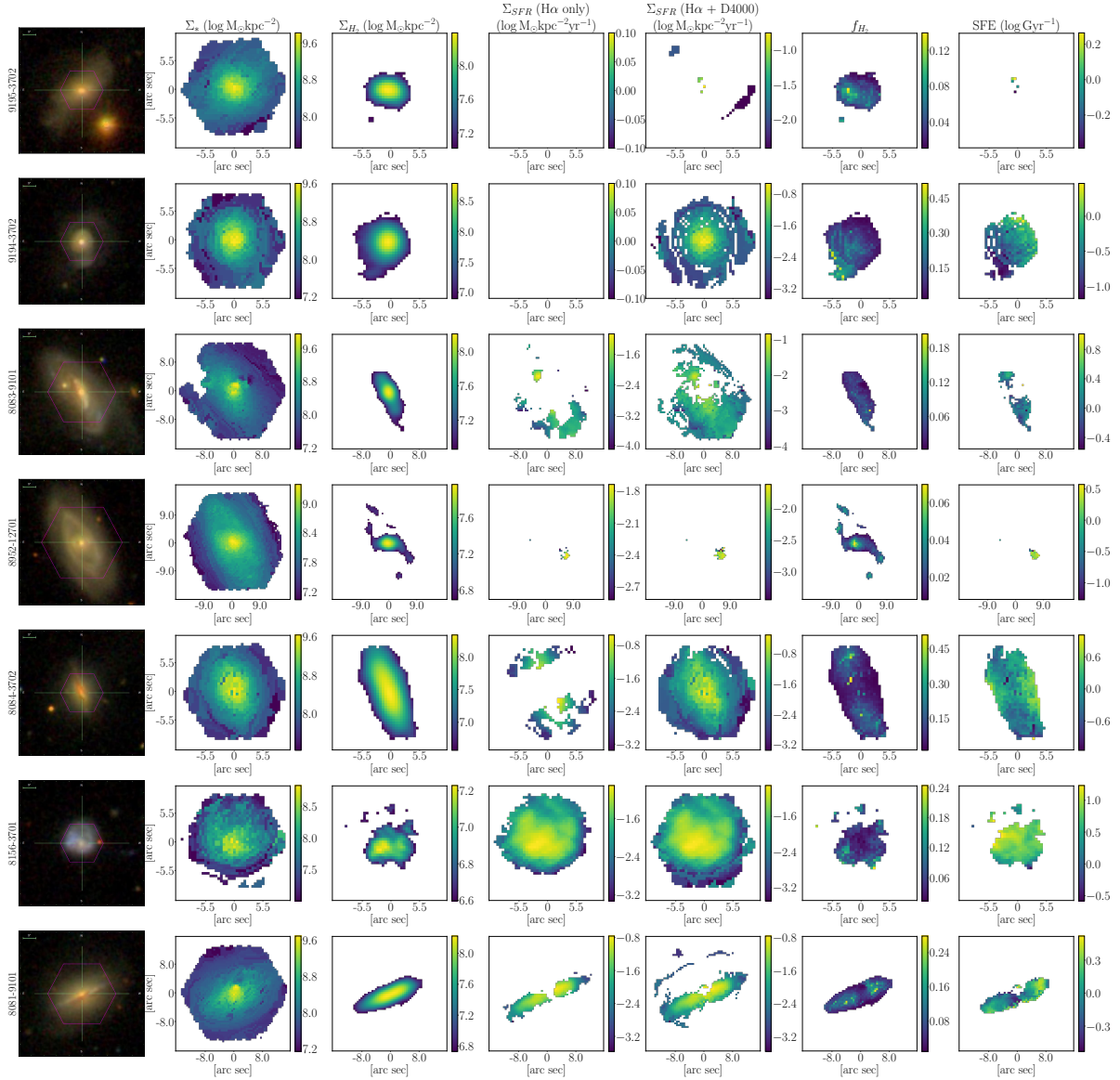


Figure A1.

highlight regions where both the new and old fuel fractions agree on the dominant mechanism: where efficiency dominates (red), fuel fraction dominates (blue), or both equally influence star formation (grey). Only two mergers change which mechanism dominates: both are mergers where efficiency and fuel are equally important with a constant α_{CO} , but then change to fuel driven. This shift is not the result of a significant change in fuel fraction, rather the two mergers were already at the border between categories. As discussed in the main analysis, these categories of “efficiency” and “fuel” driven are less robust than the continuously changing fuel fraction measurement.

In summary, our measured fuel fraction changes little when uncertainties in α_{CO} are considered. Moreover, our results concerning ΔSFE being more important to star formation than Δf_{H_2} (or vice versa) are unlikely to stem from local variations in conversion factor. Rather they characterize the true relationship between star-formation and molecular gas in a merger event.

APPENDIX C: SSFR-D4000

The SFRs presented herein include those that have been calibrated from D4000. Here, we demonstrate that our conclusions are not significantly affected by the inclusion of SFRs computed in this way. Figure C1 shows the distribution of sSFR versus D4000 for all star forming spaxels in MaNGA, based on our star forming criteria described in Subsection 2.3.1, with contours representing the density of the distribution of hexbins colour-coded by the median $\Delta \Sigma_{\text{SFR}}$ value in that bin. The asymptotic nature of the sSFR-D4000 relation as D4000 approaches 1.45 can lead to drastic difference in approximated Σ_{SFR} for spaxels with very similar D4000 values. Therefore, only spaxels with $\text{D4000} > 1.4$ are used for SFR calculations.

There is a non-negligible scatter in the sSFR-D4000 relation which is strongly correlated with $\Delta \Sigma_{\text{SFR}}$. This is to be expected; by definition a spaxel with high sSFR given the D4000 index would have a higher Σ_{SFR} given its Σ_{\star} . The red line is a median sSFR in a

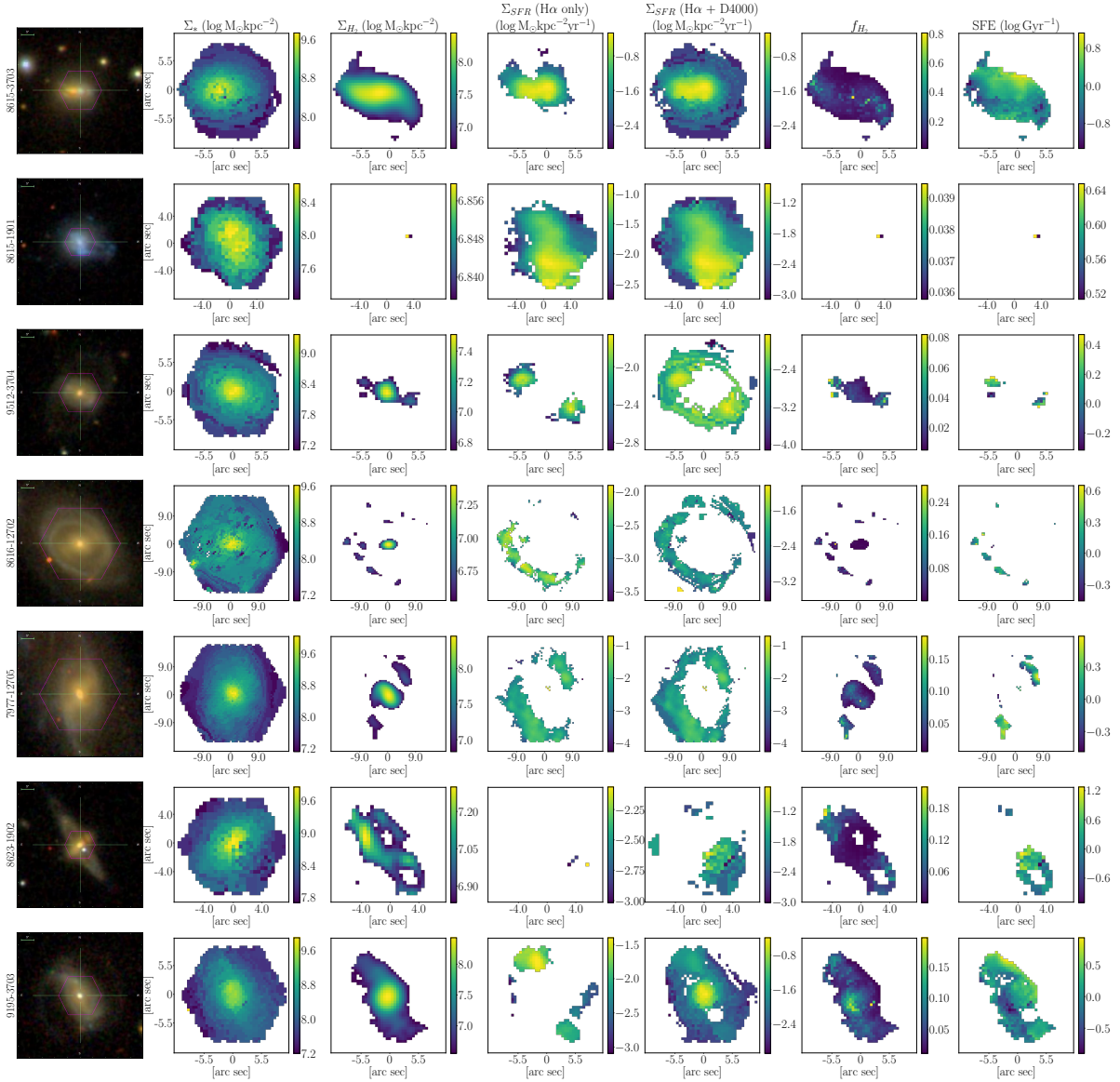


Figure A2.

bin so it makes sense that scatter significantly above the line would correspond to large, positive $\Delta\Sigma_{\text{SFR}}$. Thus by approximating Σ_{SFR} from the median sSFR, we will always underestimate the offset of the star formation from regular behaviour (both enhancements and deficits). That bias works in favour of this analysis, where we are looking for strong offsets in Σ_{SFR} . Thus for D4000- Σ_{SFR} values, any enhancement or suppression in star formation is a lower limit on the true offset; the same can be said for enhancements and deficits in SFE.

When D4000- Σ_{SFR} is used the absolute value of $\Delta\Sigma_{\text{SFR}}$ and ΔSFE will be underestimated, but Δf_{H_2} (which does not depend on a Σ_{SFR} measurement) will not be changed. The dependence of ΔSFE on Σ_{SFR} is crucial when comparing ΔSFE and Δf_{H_2} to determine which mechanism drives enhanced star formation. When using a D4000- Σ_{SFR} the value of ΔSFE is a lower limit, so $\Delta\text{SFE} > \Delta f_{\text{H}_2}$ will be consistent even if D4000- Σ_{SFR} is less accurate than H α - Σ_{SFR} . However if $\Delta\text{SFE} < \Delta f_{\text{H}_2}$, ΔSFE could be underestimated and the

statement might not be true if we could measure a H α - Σ_{SFR} . We therefore have to consider that galaxies with a large fraction of fuel driven spaxels (i.e., $\Delta\text{SFE} < \Delta f_{\text{H}_2}$) might have a smaller fraction if we were not dependent on D4000- Σ_{SFR} measurements.

To check how this bias might alter our results, we calculate the fraction of fuel driven spaxels both with our combined H α +D4000 Σ_{SFR} values, as well as those which only have H α - Σ_{SFR} . Four galaxies do not have at least 20 spaxels with viable H α - Σ_{SFR} , so can not be part of the test. Both fractions are included in Table 2 and discussed in the text, though we provide additional comparison here. Figure C2 directly compares the fuel fraction determined from only H α spaxels to the fuel fraction when both H α and D4000 spaxels are included. Ideally these two values would be equal and all galaxies would lie on the line of equality, but as expected there is some difference between the two. Difference between the two fuel fractions can be acceptable so long as it does not change which mechanism predominantly drives star formation. To better demonstrate this distinction we highlight re-

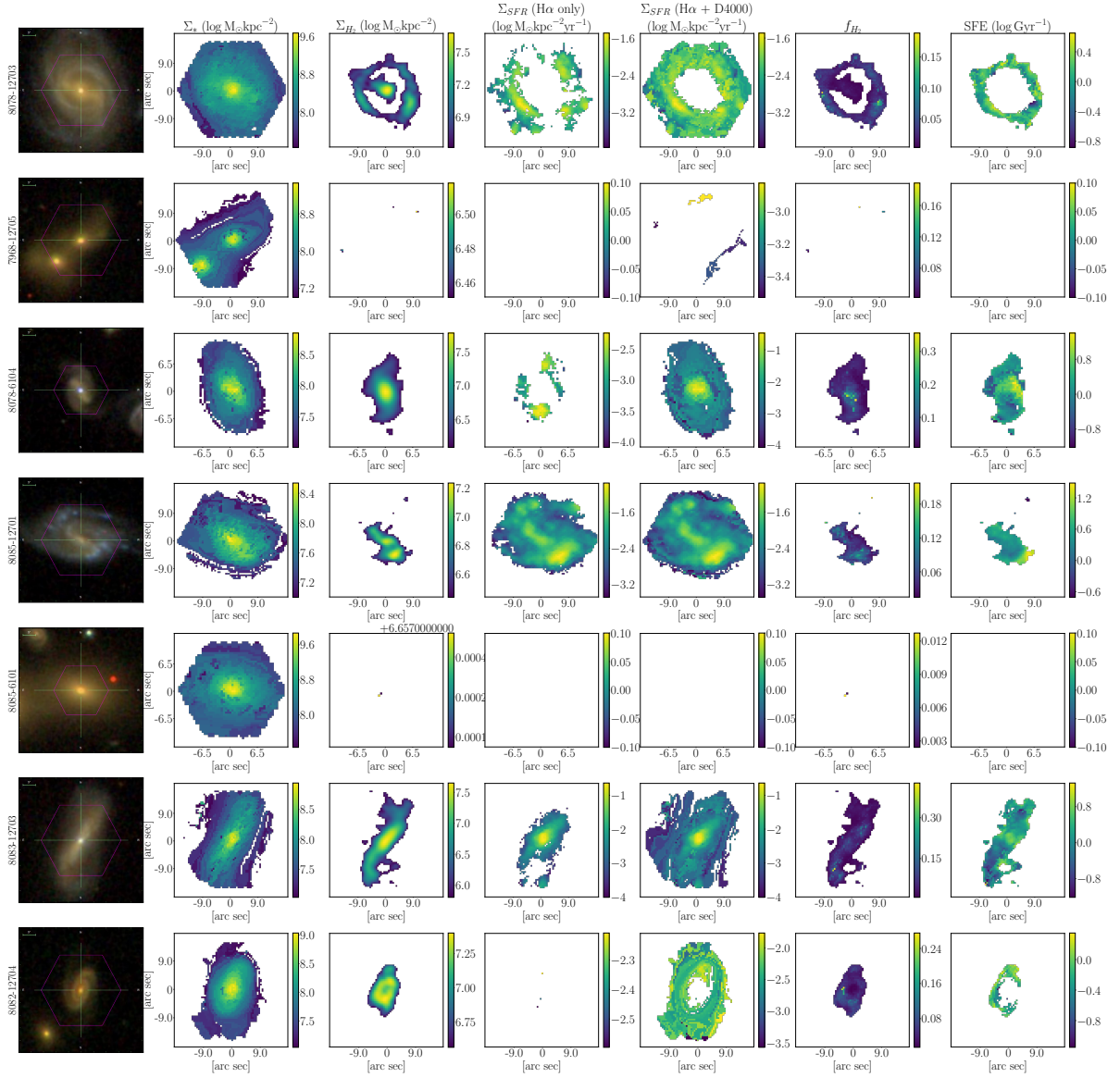


Figure A4.

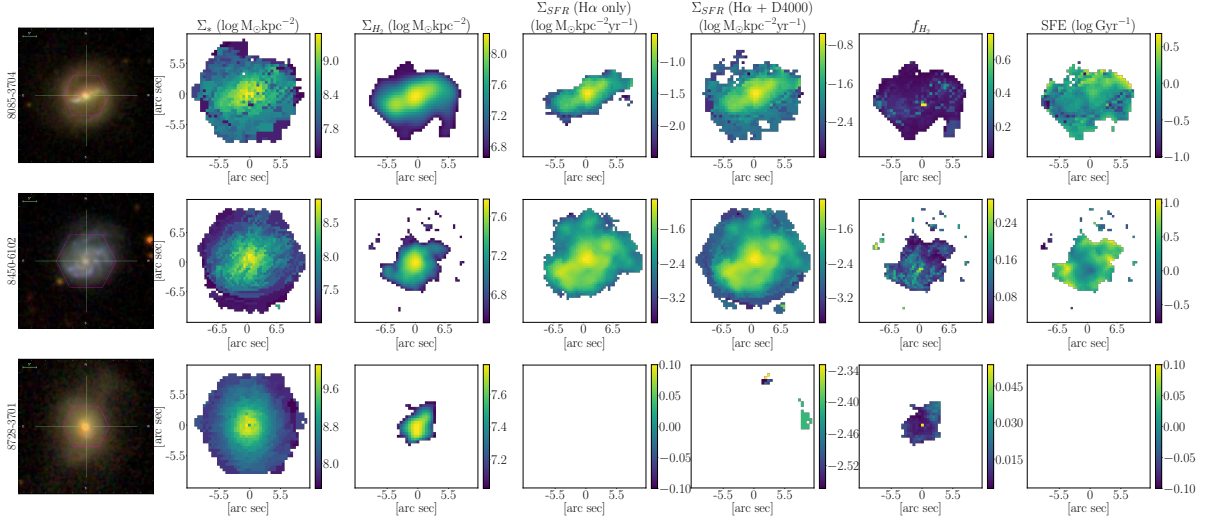


Figure A5.

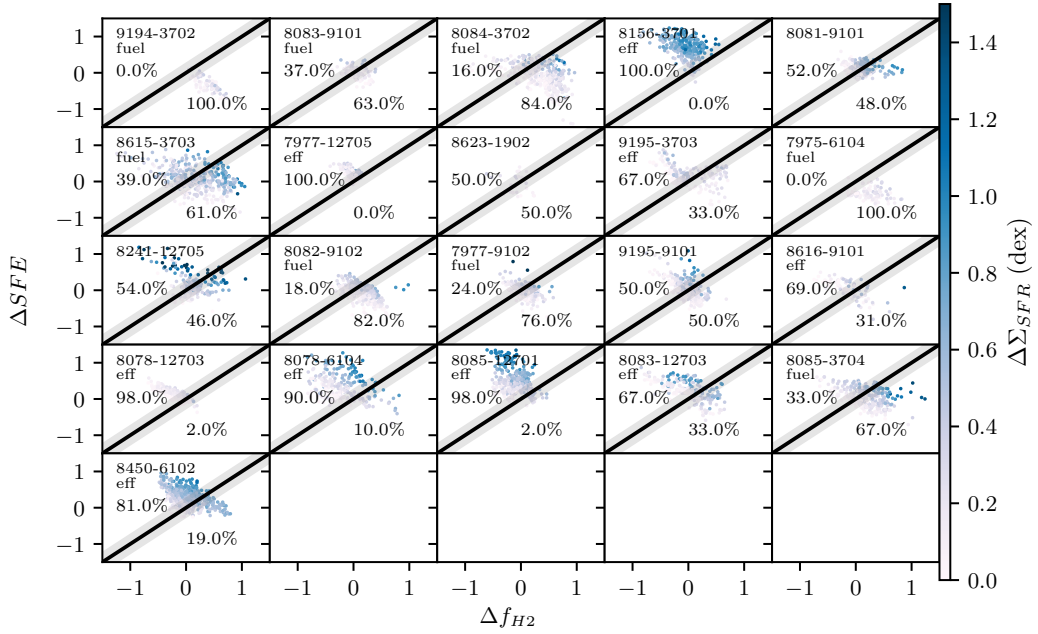


Figure B1. A replication of Figure 11, but now with a grey line indicating the 0.248 dex error on both offset parameters from using a constant α_{CO} . Pixels within this grey region are not considering when calculating the fraction of fuel driven spaxels. This biases the distribution of fuel fractions to the extreme ends (very high or very low), as spaxels further away from the line become more important in the calculation.

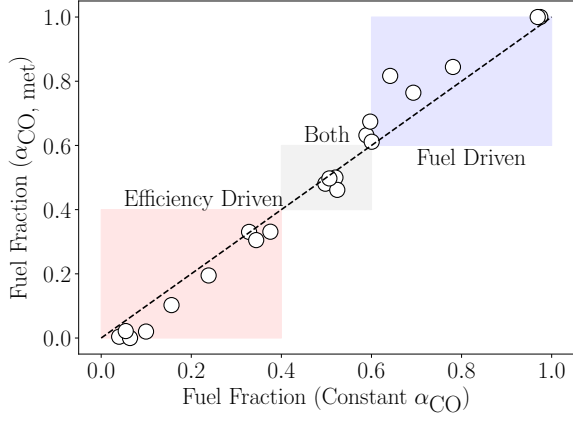


Figure B2. The fuel fraction determined from Figure B1, considering uncertainties from not using $\alpha_{\text{CO, met}}$, plot against the original fuel fraction determined from Figure 11. Note that efficiency driven mergers move below the line of equality (black dashed line), and fuel driven mergers move above the line; thus the dominant star-forming mechanism only appears more dominant when uncertainties in α_{CO} are considered. We have highlighted regions that indicate the dominant mechanism has not changed (ideally where all points would lie): where both fractions imply star formation is efficiency driven (red), where both fractions imply star formation is fuel driven (blue), and where both fractions imply star formation is driven by both (grey). Only two mergers change category (from “both” to “fuel driven”), though both galaxies were already at the border between these two categories.

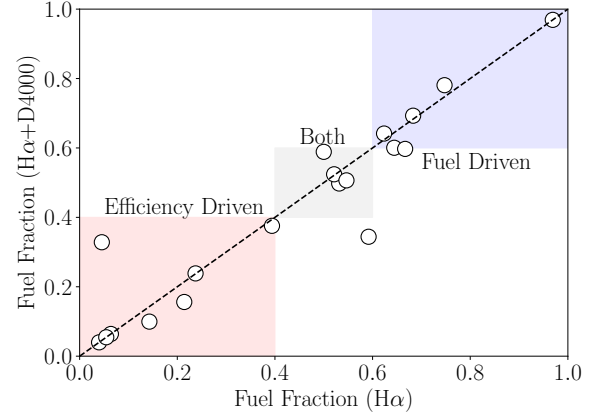


Figure C2. The fuel fraction determined from only $\text{H}\alpha$ spaxels compared to the fuel fraction when both $\text{H}\alpha$ and D4000 spaxels are included. Ideally all galaxies would lie on the line of equality, implying that the inclusion of D4000 spaxels does not drastically change our results. But realistically there is scatter about the line of equality as more spaxels are included in the analysis. Difference between the two fuel fractions is alright, so long as it does not change which mechanism predominantly drives star formation. We have highlighted regions that ideally the points should lie within: where both fractions imply star formation is efficiency driven (red), where both fractions imply star formation is fuel driven (blue), and where both fractions imply star formation is driven by both (grey). Only one point lies outside these acceptable regions: 8616-9101, which is efficiency driven when both $\text{H}\alpha$ and D4000 spaxels are included, but fuel driven when only $\text{H}\alpha$ spaxels are considered.

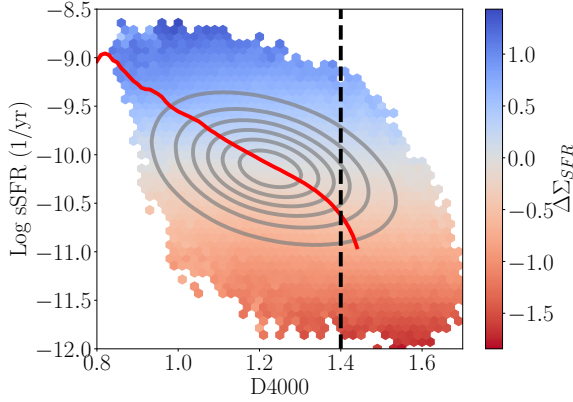


Figure C1. sSFR versus D4000 for all star forming spaxels in MaNGA. Density contours of this distribution are shown in grey, over a hexbin distribution colour-coded by the median $\Delta\Sigma_{\text{SFR}}$ value in each bin. The median sSFR value in a D4000 bin is shown in red: these points are used to approximate Σ_{SFR} for spaxels that do not meet our star-forming criteria. We exclude spaxels with $\text{D4000} > 1.4$, given the asymptotic nature of the sSFR-D4000 at high D4000. Note that there is significant scatter in this relation, which correlates with $\Delta\Sigma_{\text{SFR}}$.

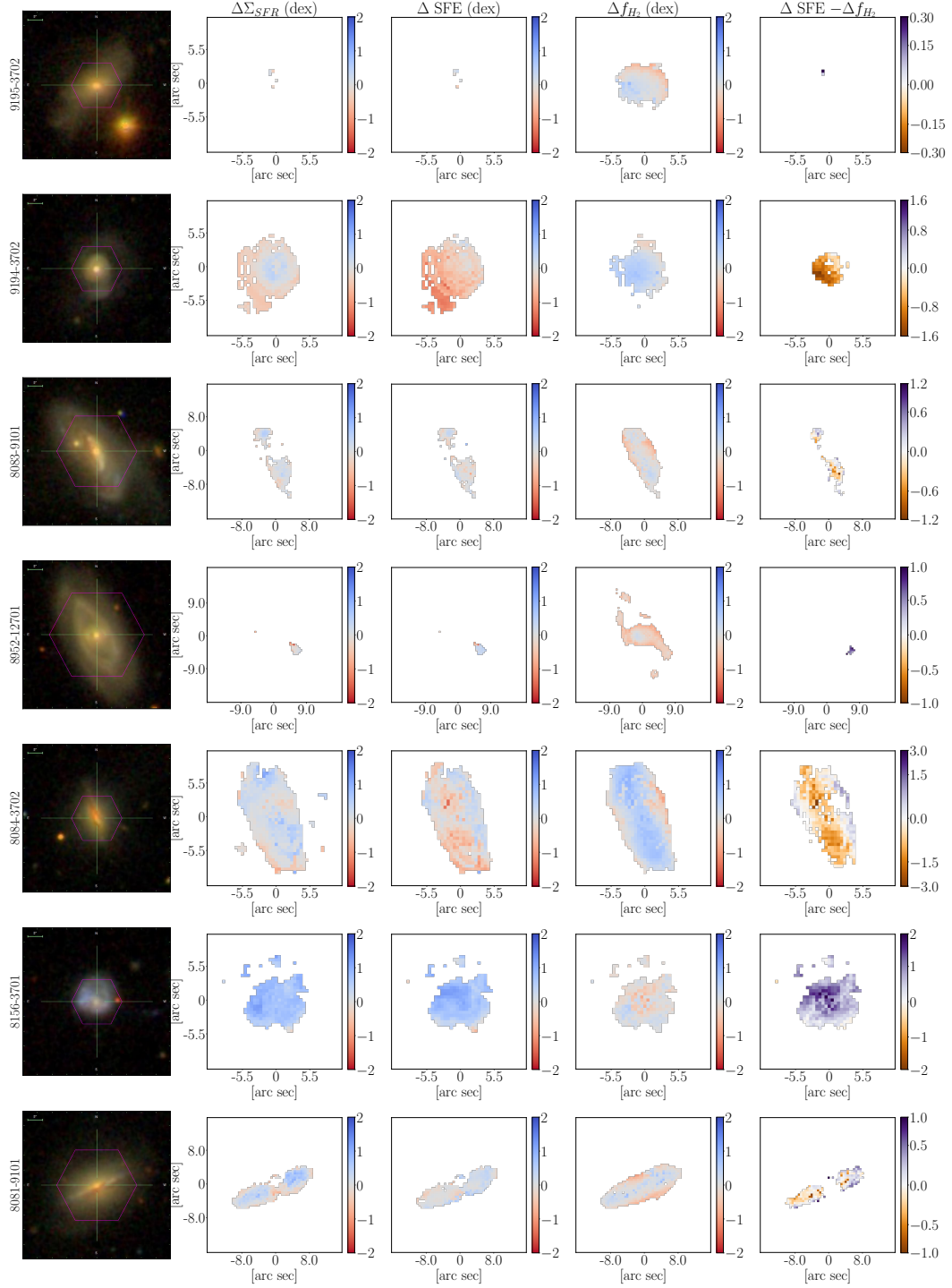
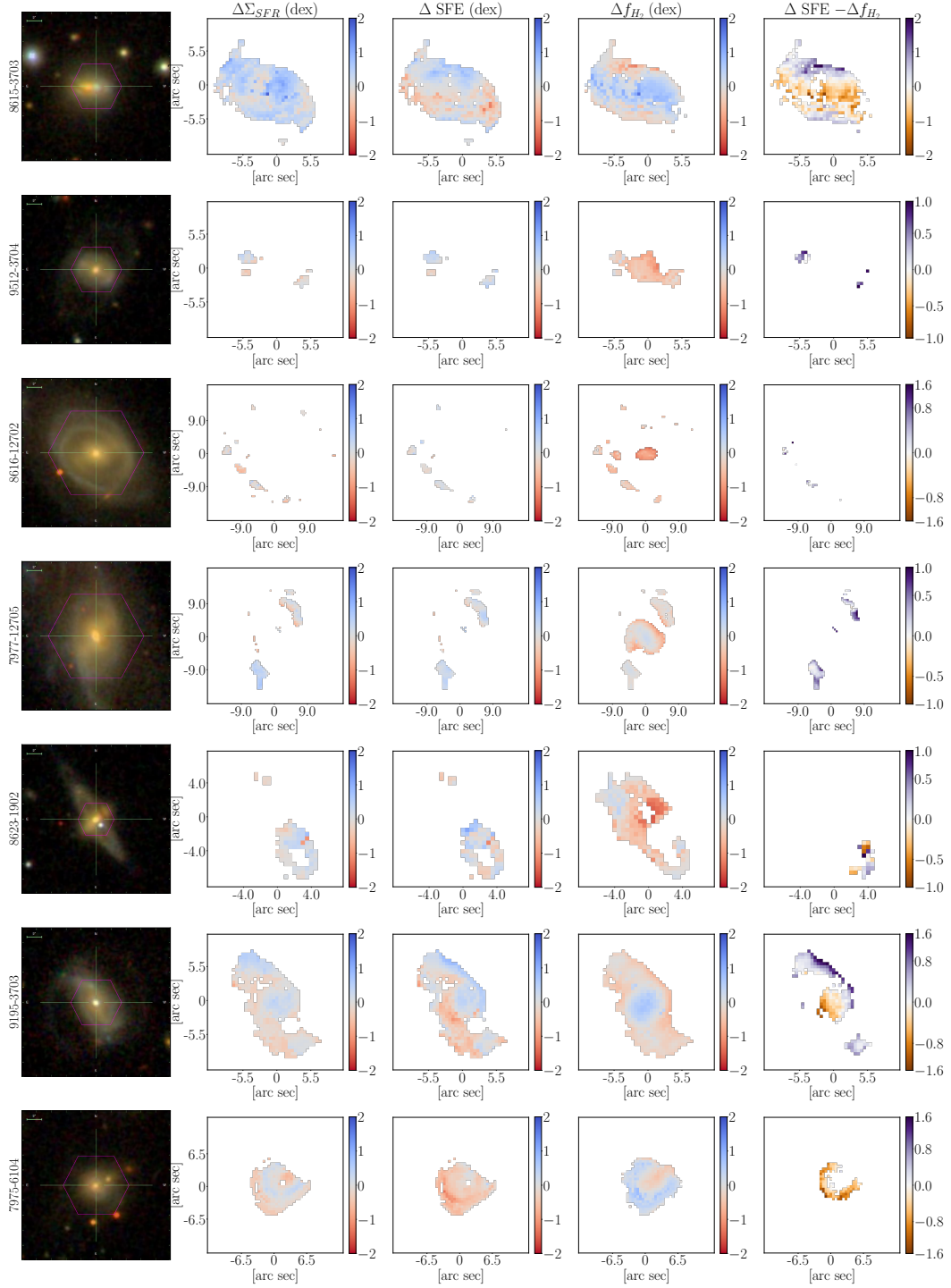


Figure D1.

**Figure D2.**

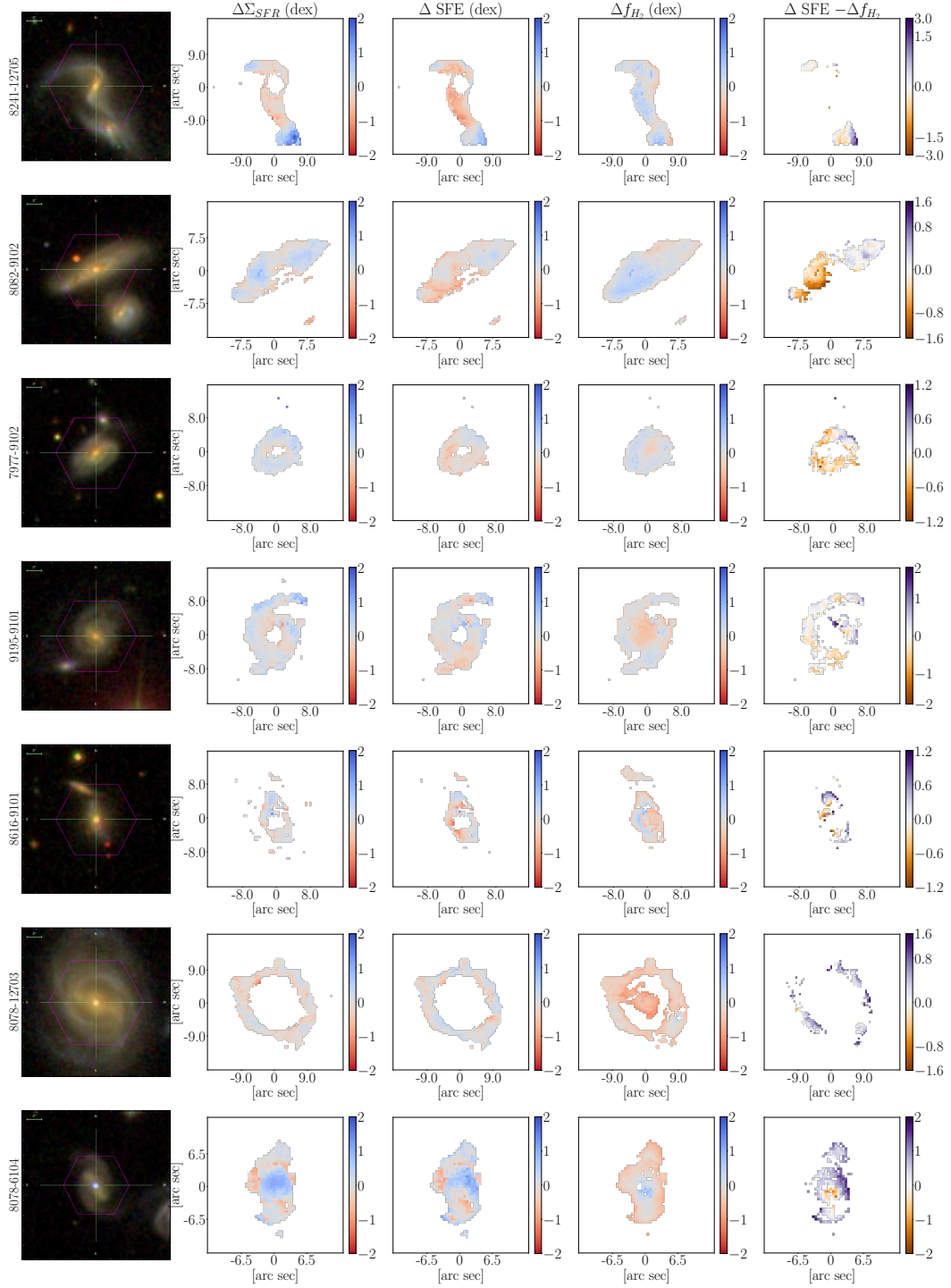
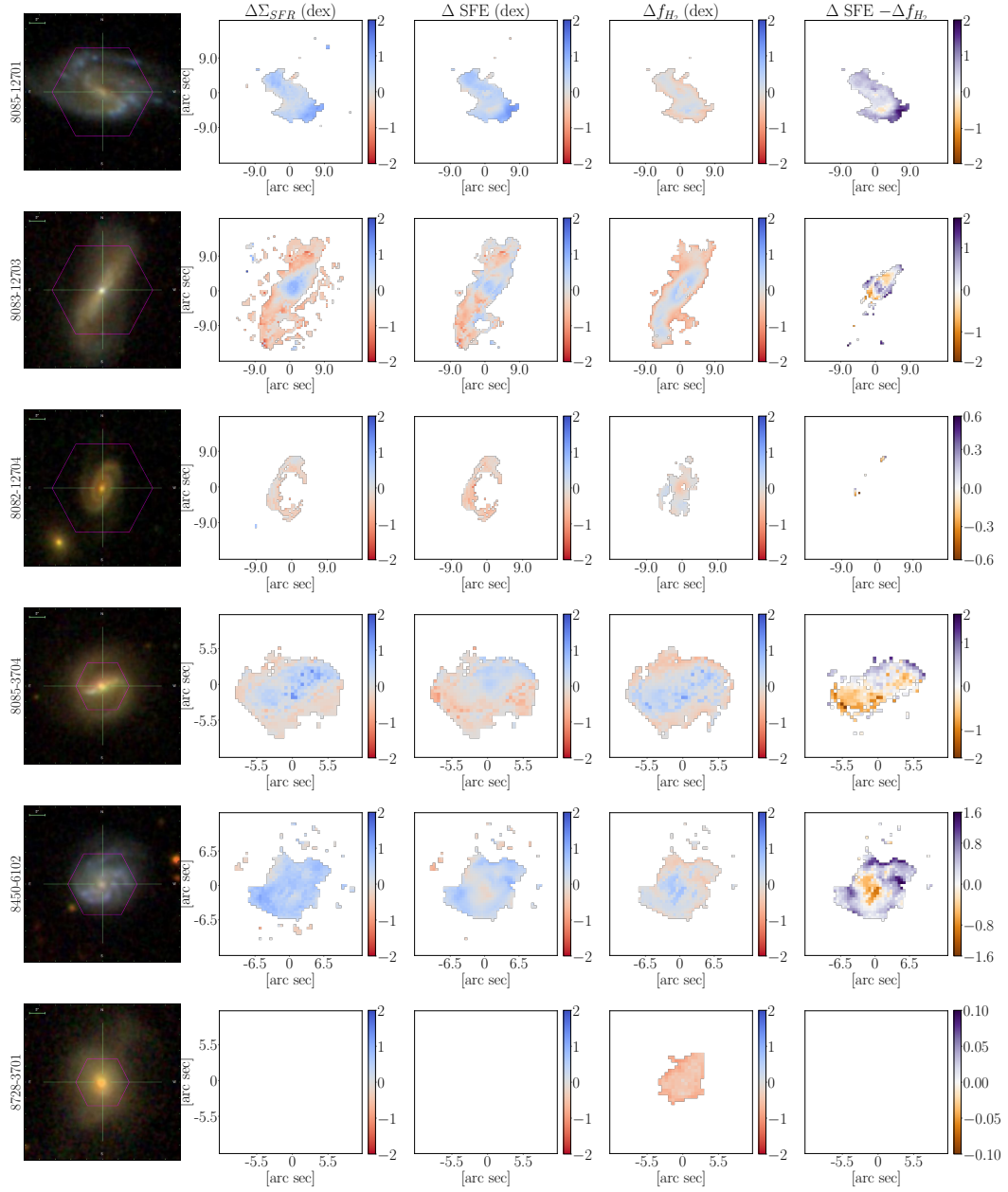


Figure D3.

**Figure D4.**